Master thesis

Non-equilibrium Solidification of δ-TRIP Steel

Choi, Young-Joo (崔暎珠)

Computational Metallurgy

Graduate Institute of Ferrous Technology

Pohang University of Science and Technology

2011

δ-TRIP강의 비평형 응고거동

Non-equilibrium Solidification of δ-TRIP Steel

Non-equilibrium Solidification of δ-TRIP Steel

By

Choi, Young-Joo
Computational Metallurgy
Graduate Institute of Ferrous Technology
Pohang University of Science and Technology

A thesis submitted to the faculty of Pohang University of Science and Technology in partial fulfillments of the requirements for the degree of Master of Science in the Graduate Institute of Ferrous Technology (Computational Metallurgy)

Pohang, Korea
December 19th, 2011

Approved by

Prof. Suh, Dong-Woo
Major Advisor

Prof. Bhadeshia, H.K.D.H.
Co-Advisor

Non-equilibrium Solidification of δ-TRIP Steel

Choi, Young-Joo

This dissertation is submitted for the degree of Master of Science at the Graduate Institute of Ferrous Technology of Pohang University of Science and Technology. The research reported herein was approved by the committee of Thesis Appraisal.

December 19th, 2011

Thesis Review Committee
Chairman: Prof. Suh, Dong-Woo
(Signature) Dongwoo Suh
Member: Prof. Kim, Han-Soo
(Signature) Hans S. Kim
Member: Prof. Cho, Jung-Wook
(Signature) Jung Wook Cho

MFT Choi, Young-Joo
20100955 Non-equilibrium solidification of δ-TRIP steel
Computational Metallurgy 2011
Advisor: Prof. Suh, Dong-Woo
Text in English

Abstract

The solidification kinetics of TRIP-assisted steels with high-aluminum contents is investigated, which is characterized by the unique microstructures containing dendritic δ-ferrite. The as-cast specimens contain higher fractions of dendritic δ-ferrite than what expected from the equilibrium phase fraction, probably for kinetic reason. Numerical simulations using DICTRA software and unidirectional solidification experiment were conducted in order to analyze the kinetic effect. However, experimentally observed ferrite fractions were higher than simulated values. Several possible factors for the discrepancy were discussed. Based on the fact that the simulation showed little changes with the cooling rate while experimentally measured ferrite fraction is increased under higher cooling rates, the accuracy of diffusivity database or the cell size set for the simulation probably is not the reason. Also, the modification in liquid diffusivity has little influence on the phase evolution. It seems that γ phase formed between the liquid and δ-phase grows more into the liquid phase due to direct solidification, resulting in considerable amount of residual δ-ferrite. The characteristic of aluminum partition, which makes liquid phase solute-depleted, is attributed to the preferred growth of γ phase toward liquid.

Nomenclature

α	Ferrite
α'	Martensite
α_B	Bainitic ferrite
α_s	Dimensionless coefficient for interdendritic back-diffusion
γ	Austenite
γ_{ret}	Retained austenite
A_{e3}	Temperature separating the α + γ and γ phase fields for a specific alloy
A'_{e3}	As A_{e3}, but para-equilibrium boundary
C_0	Initial alloy composition
C_L	Concentration of liquid phase
C_L^*	Concentration of liquid phase at the solid/liquid interface
C_S	Concentration of solid phase
C_S^*	Concentration of solid phase at the solid/liquid interface
G	Interface temperature gradient
k	Distribution coefficient
M_s	Martensite start temperature
M_d	Highest temperature to strain-induced martensite
M_s^σ	Highest temperature to stress-induced martensite

T_0	Temperature at which austenite and ferrite of the same composition have the same free energy
T_0'	As T_0, but accounting for the stored energy of ferrite
T_L	Liquidus temperature
T_q	Actual temperature given by heat flux
T_S	Solidus temperature
V	Rate of interface movement
bcc	Body-centered cubic
fcc	Face-centered cubic

Contents

Abstract i

Nomenclature ii

Contents iv

Ⅰ Introduction 1

Ⅱ Numerical Simulation 33

Ⅲ Experimental 39

3.1. Experimental procedures 39

3.2. Microscopy 41

Ⅳ Discussion 50

4.1. Solute movements 56

4.2. Partition characteristics 64

Ⅴ Conclusion 70

References 72

Acknowledgement 77

Curriculum Vitae 78

1. Introduction

As environmental concerns and issues have grown, there are concerted moves to regulate CO_2 emission. Consequently, there are many attempts to reduce exhaust fumes from cars, because they constitute major sources of CO_2 emission. Therefore it becomes important to lighten the car body and hence reduce fuel consumption. By applying higher strength steel with considerable ductility and toughness, it is possible to sustain automotive safety while maintaining a minimum weight.

The relationship between tensile strength and elongation of various steel grades is presented in Fig. 1.1. There is a general tendency of decreasing elongation with increasing tensile strength, except transformation-induced

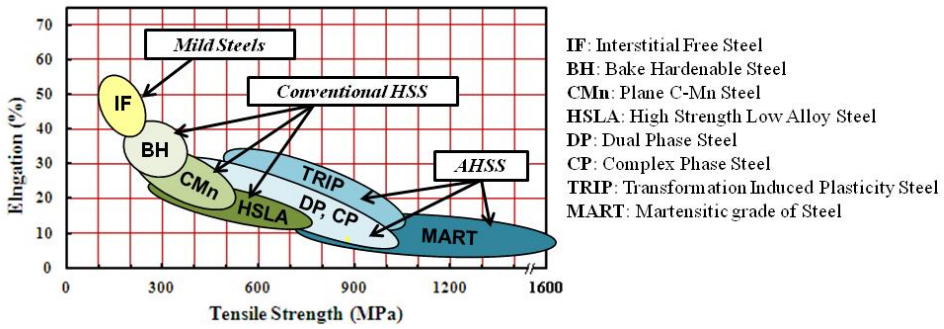

Fig. 1.1 Tensile strength and elongation of various steel grades, after Ghosh *et al.* (2008)

plasticity (TRIP) steels which have comparatively balanced properties. These promising properties are due partly to martensitic transformation from retained austenite during deformation. Various types of TRIP steels have been designed through modifying processing condition and alloying element, since it alters the microstructure and the stability of each phase.

1.1 TRIP-assisted Steels

1.1.1 TRIP-assisted Steels

TRIP-assisted steels are multiphase high-strength steels which are characterized by a large uniform elongation brought about by transformation induced plasticity during deformation. The microstructure of TRIP-assisted steel is comprised mainly of allotriomorphic ferrite, carbide-free bainitic ferrite and carbon-enriched retained austenite (Yi *et al.*, 2010).

The microstructure can be developed from cold rolled ferrite and pearlite,

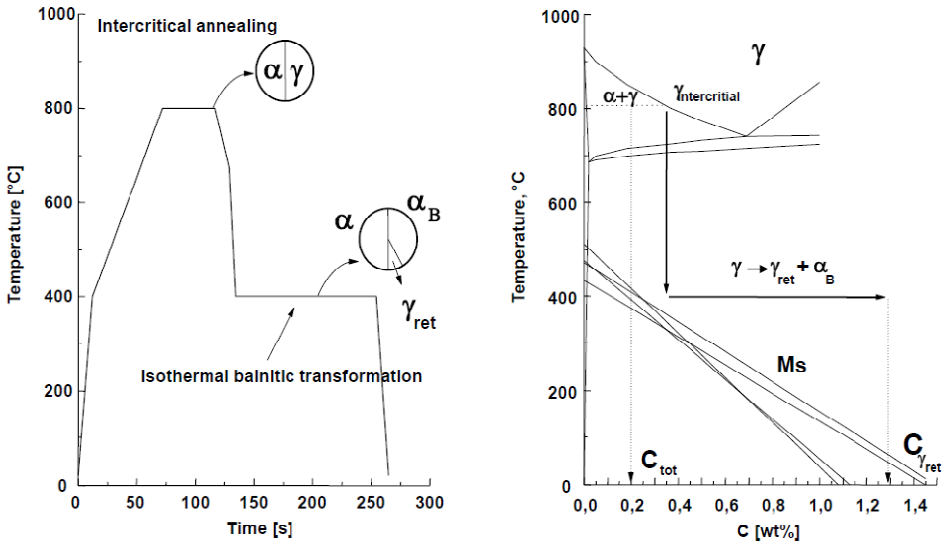

Fig. 1.2 Thermal cycle to obtain the TRIP steel microstructure (De Cooman *et al.*, 2007)

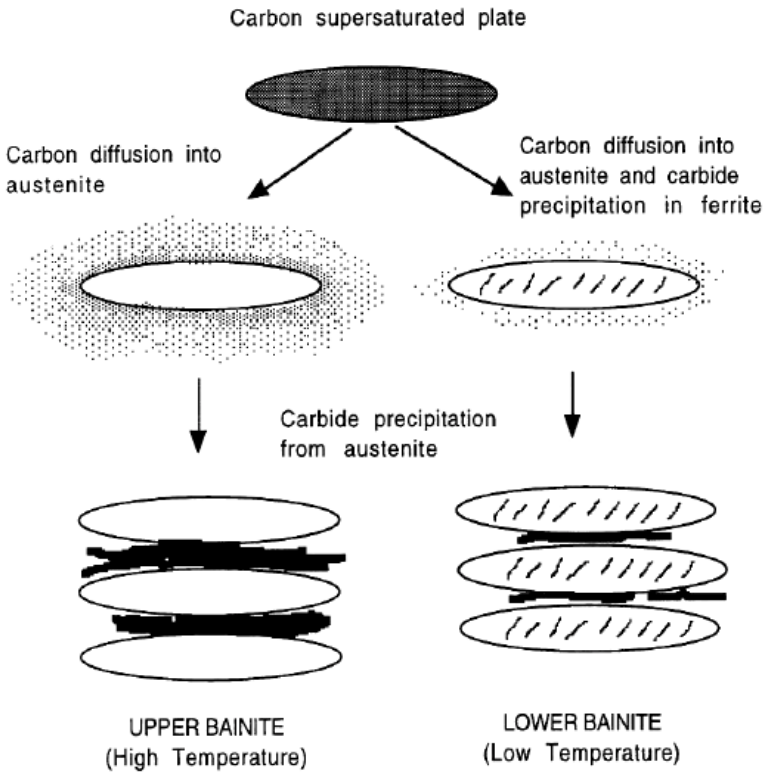

Fig. 1.3 Illustration of bainite reaction mechanism (Bhadeshia, 2001)

through intercritical annealing followed by austempering (De Cooman *et al.*, 2007). This process is shown in Fig. 1.2 and the intercritical annealing temperature determines the volume fraction of equiaxed ferrite in TRIP steel. During isothermal bainitic transformation, bainitic ferrite and carbon enriched retained austenite are formed and this process determines the volume fraction and carbon content of the retained austenite. Alternatively, hot rolled TRIP steels can be produced by control of cooling and coiling practices, which lead to ferrite formation followed by isothermal transformation into bainitic ferrite. The latter

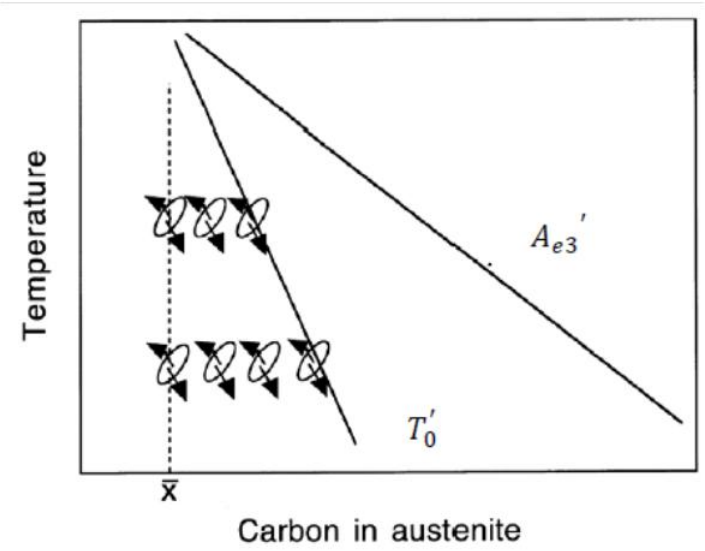

Fig. 1.4 Incomplete reaction phenomenon (Bhadeshia, 2001)

occurs at the coiling temperature and carbon-enriched retained austenite islands are left untransformed at ambient temperature. In both of these processes, the material is placed initially in the (α + γ) phase region generating a mixture of ferrite and austenite (intercritical annealing), which subsequently decomposes to bainite at a lower temperature (isothermal transformation).

The retention of austenite in TRIP-assisted steels is related closely to the movement of carbon during the bainite transformation. Bainitic ferrite forms firstly without diffusion but any excess carbon is soon afterwards rejected into the residual austenite (Fig. 1.3). The generation of the next plate of bainite, which has to grow from carbon-enriched austenite, must cease when the austenite carbon concentration reaches the $T_0{}'$ curve as shown in Fig. 1.4. This is said to

be “incomplete-reaction phenomenon”, since the austenite has not achieved its equilibrium composition at the point where the reaction stops (Bhadeshia and Honeycombe, 2006). The role of some elements which retard cementite precipitation is thus important since it bring about carbon enrichment of the residual austenite and, therefore, retention of austenite at room temperature. This was confirmed experimentally by isothermal bainitic transformation in a ~1.5 wt% silicon containing steel (Jacques *et al.*, 1999).

The retained austenite transforms into martensite during the course of plastic deformation, which gives enhanced strength and elongation to the TRIP-assisted steel (De Cooman *et al.*, 2007). The mechanical driving force due to stress or strain can make the martensitic transformation possible above the martensite-start

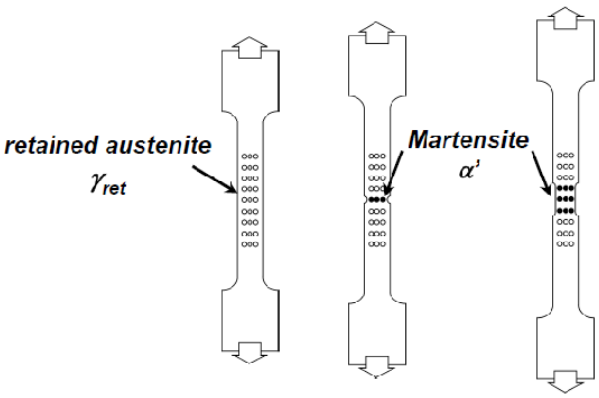

Fig. 1.5 Schematic illustration of the TRIP effect. During straining small retained austenite grains transform into high-carbon martensite, resulting in a high work hardening (De Cooman *et al.*, 2007)

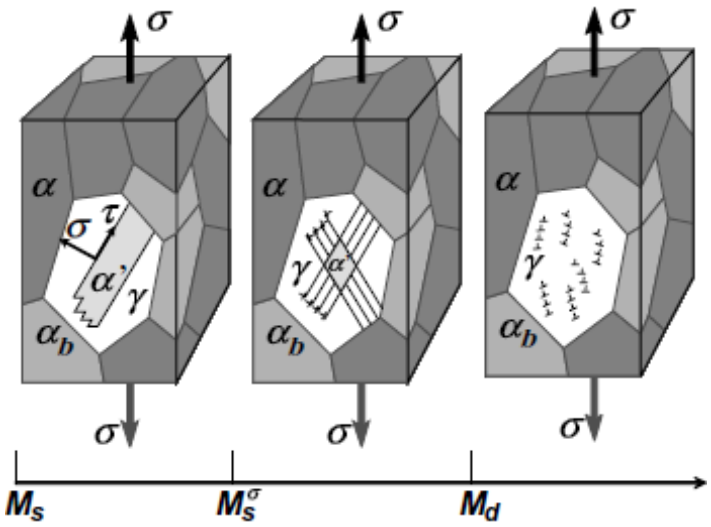

Fig. 1.6 Schematic illustration of the strain dependent yield stress (De Cooman *et al*., 2007)

temperature (M_s) as illustrated schematically in Fig. 1.5, resulting in enhanced hardening. The transformation of retained austenite into martensite is either stress or strain induced, depending on the temperature. At a temperature range between M_s and M_s^σ, yielding of the austenite is definitely by stress-induced transformation of austenite to martensite at pre-existing nucleation sites. Above M_s^σ temperature, the stress needed for promoting martensitic transformation exceeds the yield stress of the retained austenite so yielding is initiated by slip, i.e. dislocation glide. Thus strain-induced transformation occurs at new nucleation sites produced by plastic deformation in addition to pre-existing sites so that strain concentration is avoided and large uniform elongation is attained. Recent work has demonstrated that even though most assume that during plastic

deformation the $\gamma \rightarrow \alpha'$ reaction is strain induced, the evidence suggests that the major role is played by the stress that is applied in order to achieve the plastic strain. To optimize the effect of transformation-induced plasticity, the retained austenite stability is important since the beneficial effect will be reduced if the retained austenite transforms at low strains or it is very resistant to strain. The stability of retained austenite is determined by the carbon content, the size of austenite islands, the stress state and the strength of the retained austenite (Samek *et al.*, 2006).

1.1.2. Alloying elements in TRIP-assisted steel

Alloying elements are added to TRIP-assisted steels for the following reasons:

- to optimize the fraction of retained austenite,
- to control cementite precipitation,
- to increase the hardness of ferrite and
- to increase the hardenability so that pearlite formation can be avoided.

The role of carbon is critical since it can diffuse quickly and enrich the austenite. It increases the stability of austenite which can as a result be retained to below ambient temperature. The stress or strain level at which retained austenite begins to transform to martensite can be controlled by adjusting the carbon content (Yi, 2010). Carbon also has a significant effect on the amount of austenite that is retained and affects its morphology (Chen *et al.*, 2002).

The stabilizing effect of carbon is available only if carbon is not consumed by

the formation of cementite, hence it is important to control the precipitation of cementite. One of the alloying elements involved in cementite formation kinetics is silicon. It is found that the cementite precipitation in austenite is remarkably retarded when a small concentration of silicon is added, which can be explained by the fact that the cementite traps the silicon as it grows when it forms under paraequilibrium conditions. As a consequence, the free energy change of the reaction is reduced so that the kinetics of precipitation slows down (Kozeschnik and Bhadeshia, 2008). However, a high silicon content is detrimental to the galvanizability of steel strips since it segregates to the surface and obstructs the formation of an inhibition layer (Mahieu *et al*., 2001).

Aluminum additions also retard the rate of cementite precipitation since like silicon, it has negligible solubility in cementite (Leslie and Rauch, 1978). There have been several attempts to substitute silicon with aluminum since aluminum does not segregate as a solute hence is not expected to influence the coatability adversely (MEYER *et al*., 1999, MAHIEU *et al*., 2002). These authors found out that aluminum substituted C – Mn – Si TRIP alloys showed good mechanical properties, although high contents of aluminum (~1.7 wt%) is needed to suppress effectively the pearlite formation.

Niobium is known to improve elongation and strength (HASHIMOTO *et al*., 2004), when added about 0.05 wt%. Also, the multiple addition of 0.2 wt% molybdenum with 0.05 wt% niobium results in higher tensile strength by the large amount of fine NbMoC precipitates.

1.1.3. δ-TRIP steel

A combination of neural networks and genetic algorithms has been used to design a TRIP assisted steel which has an optimum quantity of retained austenite and yet minimum silicon concentration (Chatterjee *et al*., 2007). The composition of steel was optimized as shown in Table 1.1 and then manufactured in an as-cast condition. The fractions of the equilibrium phases of the alloy were calculated using MT-DATA with the SGTE database, which is shown in Fig. 1.7. The diagram shows that a fully austenitic state cannot be achieved at any temperature, so that dendritic δ-ferrite would persist in the cast alloy. Fig. 1.8a shows the novel microstructure consisting of δ-ferrite dendrites and a residual phase which at high temperatures is austenite. The austenite evolves into a mixture of bainitic ferrite and carbon enriched retained austenite with appropriate heat treatment, as shown in Fig. 1.8b. In the microstructure, the stable dendritic δ-ferrites replace the allotriomorphic ferrites found in conventional TRIP assisted alloys. It is therefore designated as δ-TRIP steel (Chatterjee *et al*., 2007). The properties of heat treated specimens exhibited a 23% total elongation and an ultimate tensile strength of 1000 MPa.

Alloy	C	Si	Mn	Al	Cu	P
Optimum	0.4	0.5	2.0	2.0	0.5	0.02
experimental	0.36	0.73	1.96	2.22	0.52	0.022

Table 1.1 Chemical composition of model perceived optimum alloy and experimental alloy, wt% (Chatterjee *et al.*, 2007)

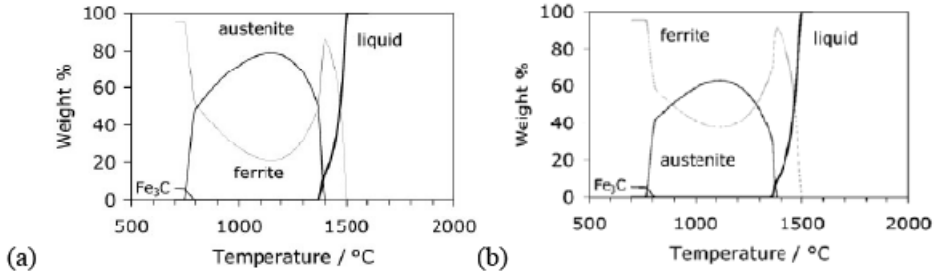

Fig. 1.7 Calculated quantities of phases as function of temperature (Chatterjee *et al.*, 2007)

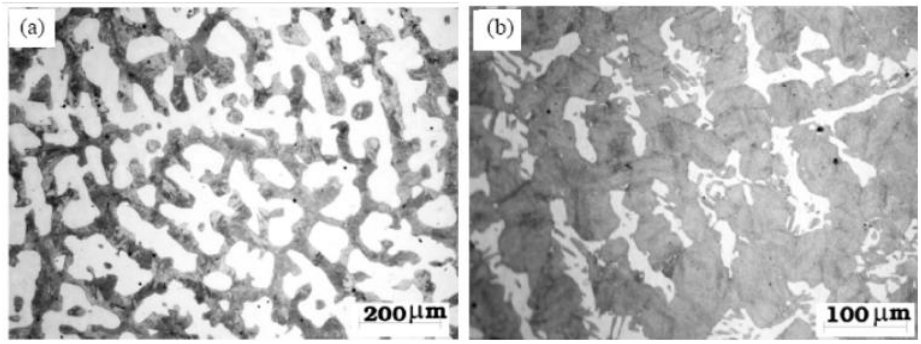

Fig. 1.8 Microstructure of the alloy (a) as-cast (b) heat treated (Chatterjee *et al.*, 2007)

1.2 Solidification Kinetics

1.2.1. Solidification Microstructure

There is a variety of solidification microstructures according to the solidification conditions and the material of interest. Almost all of the solidification microstructures can be divided into single-phase primary crystals and polyphase structures which evolve subsequently. The morphology of single-phase primary crystals changes with the growth direction, temperature gradient and growth rate. In case of polyphase structure which is also called eutectic morphology, two or more phases grow simultaneously from the liquid. The following discussion will be focused on the morphology and the scale of single-phase structure since it is more related to the subject.

In a pure substance, interface instability is determined by the heat flow direction and solid growth directions as illustrated in Fig. 1.9 (Kurz and Fisher, 1986). If the solid phase grows inward from the mold wall, the heat flow occurs in the opposite direction of that of the solid growth, forming positive temperature gradient. When a perturbation forms at an interface under this condition, the temperature gradient in the liquid increases while that in the solid decreases. As a result, more heat flows into protruding part of the perturbation and thus the perturbation melts back, making planar interface stabilized. On the other hand, if the free crystals grow radially into an undercooled melt, there forms negative temperature gradient in the liquid, thus heat flow occurs in the same direction as

solid growth. In this case, a perturbation formed on the interface ends up in even more undercooled liquid so that the interface becomes unstable and dendritic crystals forms, which is called thermal dendrite.

In the case of alloys, the variation in the local equilibrium melting point should be considered since solutes will pile up ahead of the interface. As the liquid concentration increases around interface, the liquidus temperature of the alloy will decreases according to the phase diagram, as shown Fig. 1.10. When the slope of the local melting point curve is greater than that of the actual temperature gradient, the tip of growing solid encounters constitutional

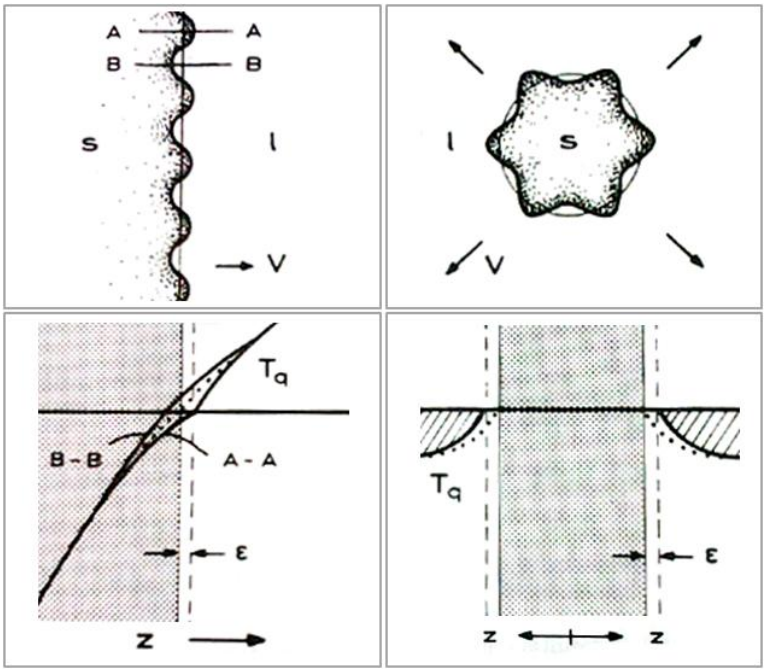

Fig. 1.9 Columnar and equiaxed solidification (Kurz and Fisher, 1986)
ε is the amplitude of a perturbation and T_q is the temperature given by heat flux

undercooling. As a result, the interface becomes unstable and perturbations grow up. This leads to the development of cellular structure as shown Fig. 1.11a during directional growth of alloy. The initial cellular structures are adjusted to a more optimum spacing according to the dissipation of piled-up solutes and heat flow. Furthermore, the larger cells which have a slightly perturbed surface may cause intercellular instability which might possibly lead to dendrite formation. The dendrite growth direction is closely related to the crystal orientations due to the anisotropy of solid/liquid interface energy and growth kinetics while the cells are grown parallel to the heat flow direction. In the case of cubic crystals, [001] is

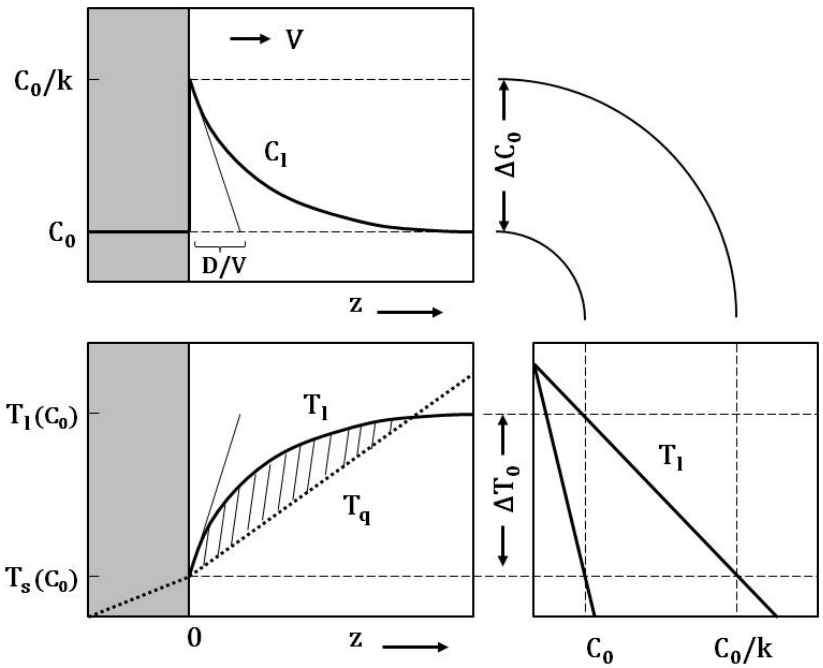

Fig. 1.10 Constitutional undercooling in alloys (Kurz and Fisher, 1986)

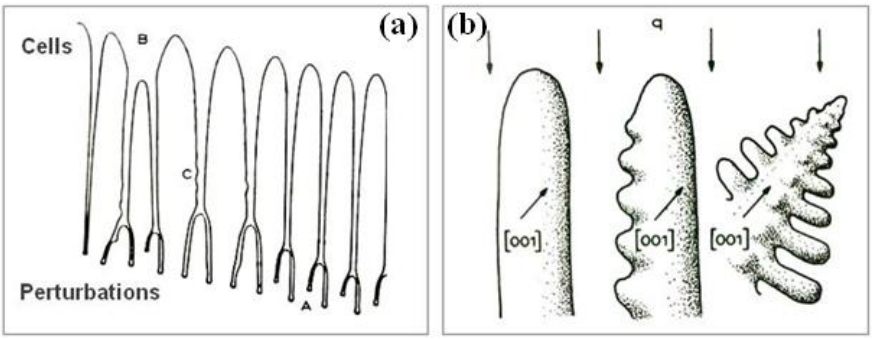

Fig. 1.11 (a) breakdown of a plane solid/liquid interface to give cells (b) cells, dendritic cells, and dendrites (Kurz and Fisher, 1986)

the preferred growth orientation and dendrites will grow more in the preferred direction which is closest to the heat flow direction, as shown Fig. 1.11b.

The scale of the microstructure can be represented by dendrite arm spacing for columnar dendrites. Primary dendrite arm spacing decreases with the increase in the temperature gradient or growth rate. When a perturbation occurs and the solid/liquid interface becomes unstable, secondary arms start to form from the tip

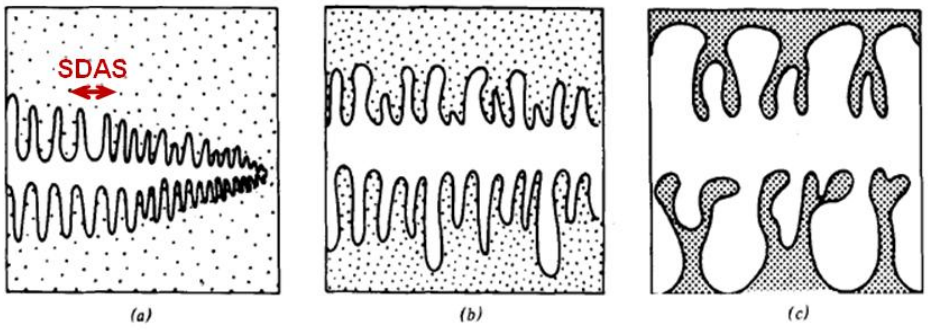

Fig. 1.12 Growth of a dendrite (Flemings, 1974a)

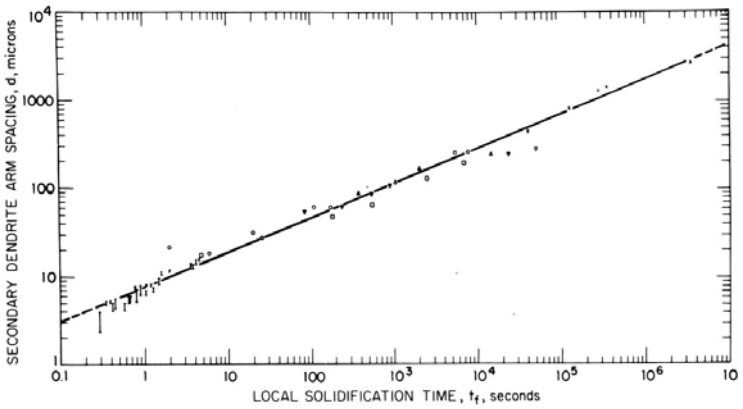

Fig. 1.13 Secondary arm spacing as a function of solidification time (Bower *et al*., 1966)

of primary dendrite. The important aspect of the secondary dendrite arm spacing (SDAS) is that it changes with the time through coarsening while primary dendrite arm spacing remains unchanged once it formed.

When a secondary dendrite is growing into a melt as shown in Fig. 1.12, fine dendrite arms form firstly and some coarsen as solidification proceeds. This process is analogous to Ostwald ripening and the final SDAS is determined by the time permitted to proceed with the process (Flemings, 1974a). If a higher cooling rate is applied, there is less time for coarsening and the spacing will be finer. This is confirmed by plots of dendrite arm spacing versus cooling rate for a wide variety of alloys that shows strong dependence of SDAS and cooling rate. They are linear on a log-log plot with a slope of between -1/2 and -1/3 and an example of the plots is shown in Fig. 1.13. This means that SDAS is strongly and solely dependent on cooling rate and the relationship can be used to estimate the

cooling rate during solidification (Flemings, 1974a).

In summary, the two major variables that determine solidification microstructure under given composition are temperature gradient, G, and growth rate, V. The scale of microstructure depends on $G \cdot V$, which is equivalent to the cooling rate under unidirectional heat flow. On the other hand, the morphology is determined by G/V, from planar, to cellular, to dendritic growth (Kurz and Fisher, 1986).

1.2.2. Microsegregation

The formation of a crystal from an alloy melt causes a local change in the composition. The difference in the composition can be described by the distribution coefficient k under isothermal and isobaric conditions, as shown in Fig. 1.14 and Eq. 1.1. The solidus and liquidus lines will be assumed to be

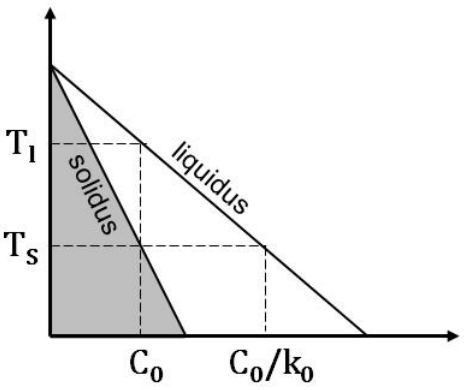

Fig. 1.14 Solid/liquid equilibrium

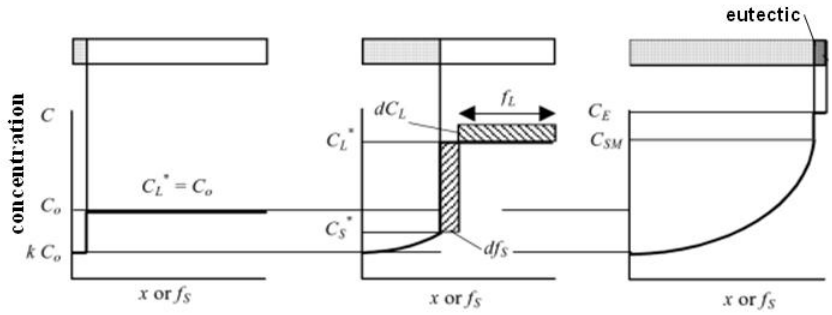

Fig. 1.15 Solute redistribution during solidification with Scheil-Gulliver approximation. The volume element is set to the section across half of a dendrite arm freezing within the mushy zone (Stefanescu, 2002)

straight for simplicity, which means that k is constant.

$$k = \left(\frac{C_S}{C_l}\right)_{T,P} \tag{1.1}$$

Assuming that the local equilibrium exists at the interface and the distribution coefficient is less than unity as in the general cases, solutes will be rejected into the liquid phase. Under equilibrium solidification conditions where the rate is slow enough to allow sufficient diffusion within the system, the composition of the last liquid remaining at T_s will be C_0/k_0 and the solid will have the composition of C_0 after solidification is completed. This condition is consistent with the application of the lever rule to the equilibrium phase diagram.

However, it is very difficult to meet the equilibrium solidification condition since the diffusion rate in the solid phase is relatively slow. The Scheil-Gulliver equation assumes complete mixing of solute in the liquid and no diffusion in the

solid phase. Since solute is rejected from the growing solid into the remaining liquid as shown in Eq. 1.2, the composition of the growing solid gradually increases as solidification proceeds and it results in a high level of segregation at the end of the process. The composition of each phase is given in Eq. 1.3, which can be obtained by integrating Eq. 1.2 (Kurz and Fisher, 1986).

$$(C_L - C_S)\mathrm{d}f_S = (1 - f_S)\mathrm{d}C_L \tag{1.2}$$

$$(C_S^* = k_0 C_0 \text{ at } f_s = 0)$$

$$C_S^* = k_0 C_0 (1 - f_S)^{(k_0 - 1)}$$

$$C_L = C_0 f_L^{(k_0 - 1)} \tag{1.3}$$

where C_L is the composition in the liquid, C_S in the solid, C_S^* in the solid at the interface and f_s is solid fraction. The solute redistribution is illustrated in Fig. 1.15 where f_L is liquid fraction and C_E is the eutectic composition.

In the absence of complicating factors, the solute distribution is expected to lie between the above two extremes, depending on the amount of solid state diffusion. Brody and Flemings (1966) have presented an analysis which quantifies the effect of solid state diffusion as illustrated in Fig. 1.16. During a small increment of solidification of an alloy of mean composition C_0, solute rejected at interface diffuses into solid and liquid (Eq. 1.4),

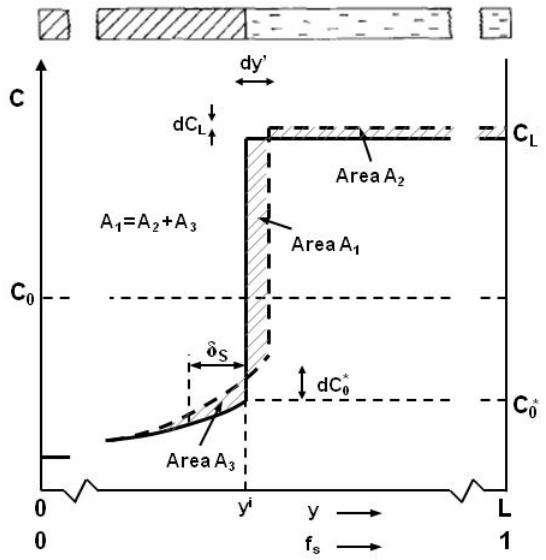

Fig. 1.16 Solute redistribution during incremental freezing in a volume element of length L, considering the back-diffusion of solutes (Clyne and Kurz, 1981)

$$(C_L - C_s^*)L\mathrm{d}f_s = L(1-f_s)\mathrm{d}C_L + \frac{1}{2}\delta_s \mathrm{d}C_s^* \tag{1.4}$$

where the back-diffusion solute boundary layer is given by

$$\delta_s = \frac{2D_s}{V} \tag{1.5}$$

in which D_s is the solute diffusivity in the solid and V is the local interface advance velocity. With the hypothesis of a parabolic decrease in V with increasing time, the integration of the Eq. 1.4 leads to:

$$C_s^l = kC_0\{1-(1-2\alpha k)f_s\}^{(k-1)/(1-2\alpha_s k)} \tag{1.6}$$

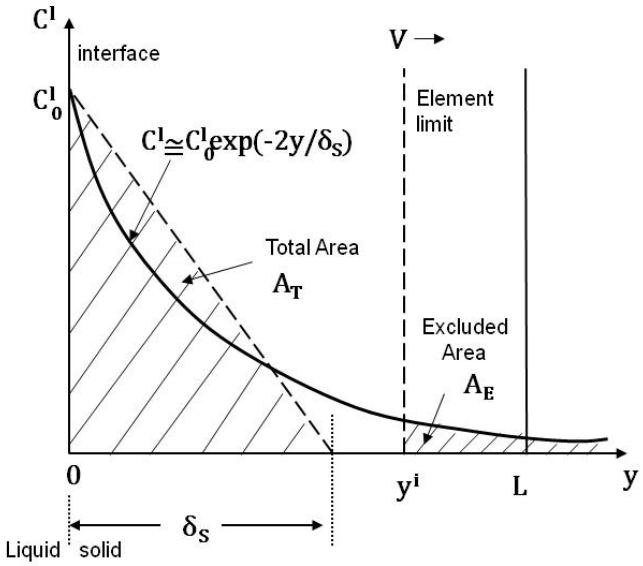

Fig. 1.17 Composition difference between the pre-existing profile and that after incremental interface advance versus distance back from the interface. The curve is approximated to exponential decay (Clyne and Kurz, 1981)

where

$$\alpha_s = \frac{4D_s t_f}{L^2} \tag{1.7}$$

and t_f is total solidification time.

It is notable that substituting $\alpha_s = 0$ (no diffusion in the solid) into Eq. 1.6 reduces it to the Scheil-Gulliver model. One would also anticipate that $\alpha_s = \infty$ would produce the lever rule, however, setting $\alpha_s = 0.5$ recovers the lever rule since Brody-Flemings model does not conserve solute in the solid. The problem has been elaborated by Clyne and Kurz (1981) who tried to quantify the error caused by the cutoff effect. The excluded area A_E in Fig. 1.17 illustrates the

fraction of back diffusion solute cut off by the physical limits of the volume element during local solidification period. They introduced the parameter Ω including the effect of solute cut off, which is close to the lever rule in the limit as $\alpha_s = \infty$. The fraction of solid predicted by Clyne-Kurz model is presented in Fig. 1.18.

For the segregation behavior of multi-component alloys, many works have been done using numerical method (Ueshima *et al*., 1986, Natsume *et al*., 2010, Das *et al*., 1999). Although there are many different assumptions and different geometries of volume element, the calculation is basically made by dividing the volume element into small parts, each of which is called a node (Fig.1.19). Then the rate of diffusion into each phase is calculated as time Δt passes and temperature ΔT decreases. One of the flow charts for the calculation of solute distribution is presented in Fig. 1.20.

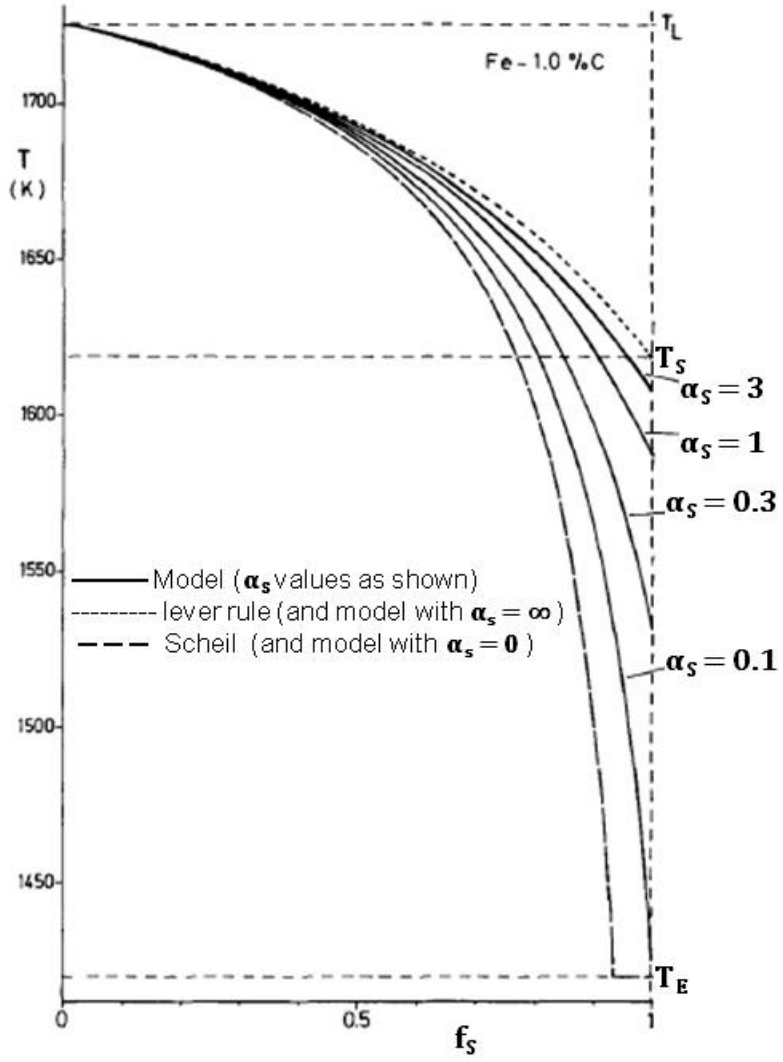

Fig. 1.18 Predicted fraction of solid versus temperature for Fe − 1.0C wt% alloy according to the classical limiting cases and the proposed model (Clyne and Kurz, 1981)

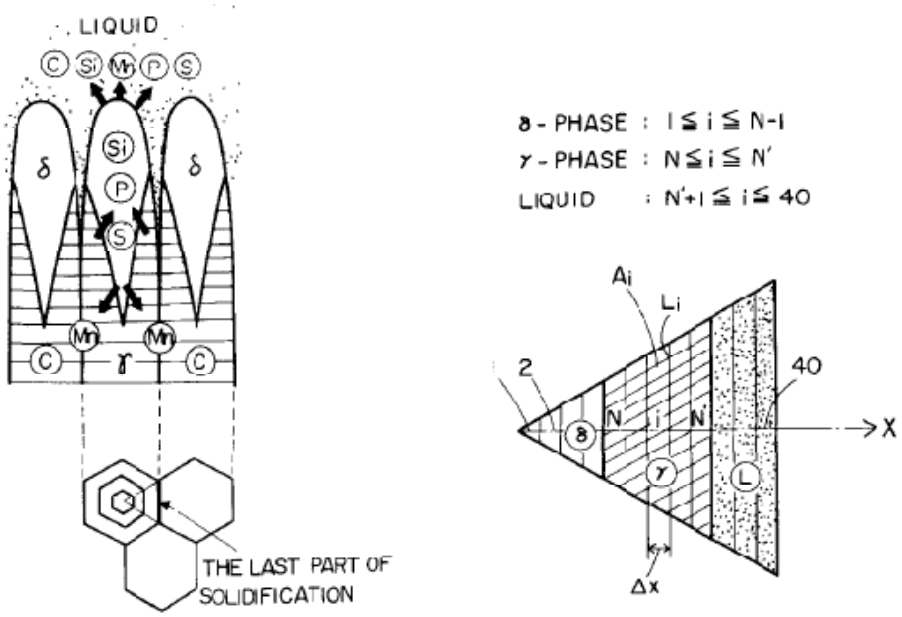

Fig. 1.19 Schematic drawing showing the longitudinal and transverse cross sections of dendrites (left), a part of transverse cross section of dendrite (right) (Ueshima *et al*., 1986)

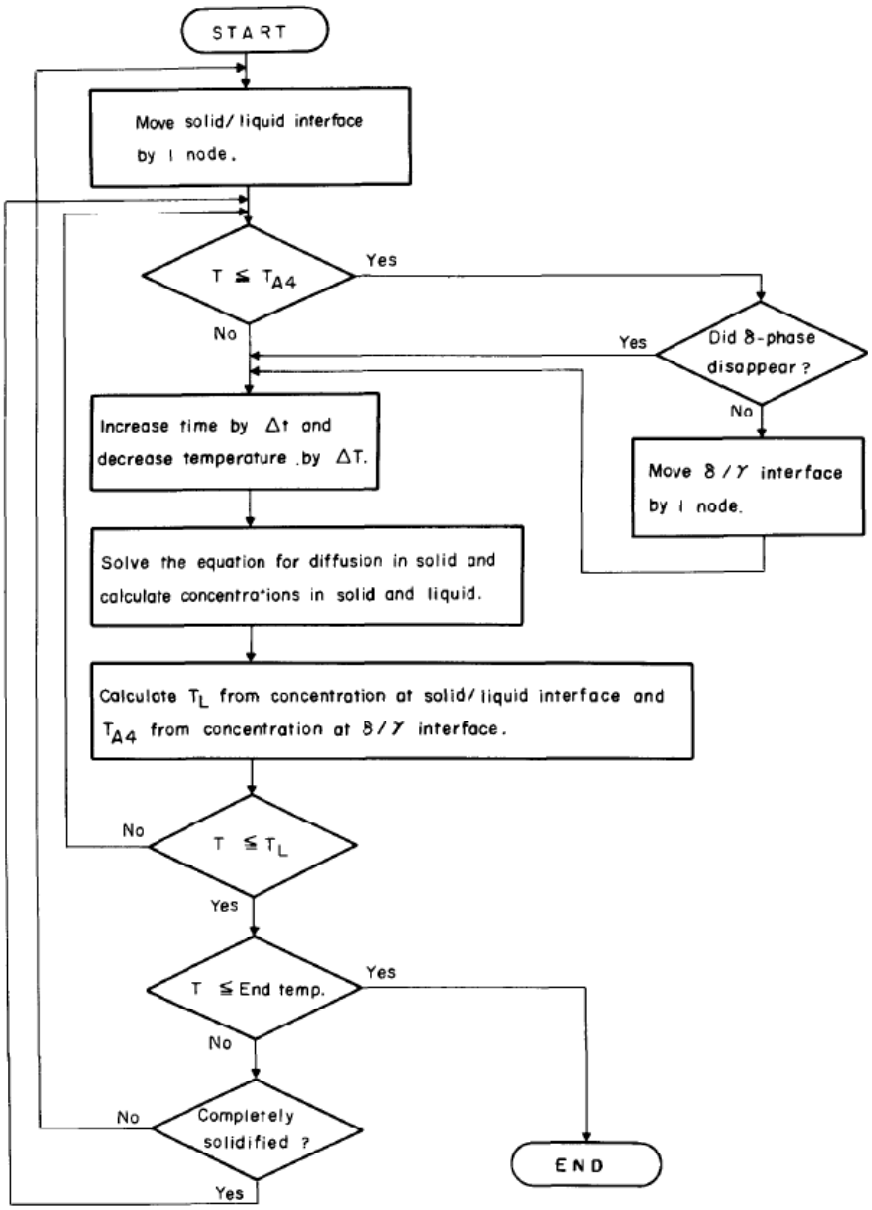

Fig. 1.20 Flow chart for the calculation of solute distribution (Ueshima *et al*., 1986)

1.2.3. Peritectic Solidification

In the peritectic transformation, liquid and solid phase react to form another solid. Since the transformation involves reactions among three phases and terms have been used inconsistently, it is pertinent to clarify each reaction. According to Kerr *et al.* (1974), the peritectic phase transition consists of two separate stages: the peritectic reaction followed by the peritectic transformation. The peritectic reaction occurs when the liquid, δ-ferrite and austenite phases are in

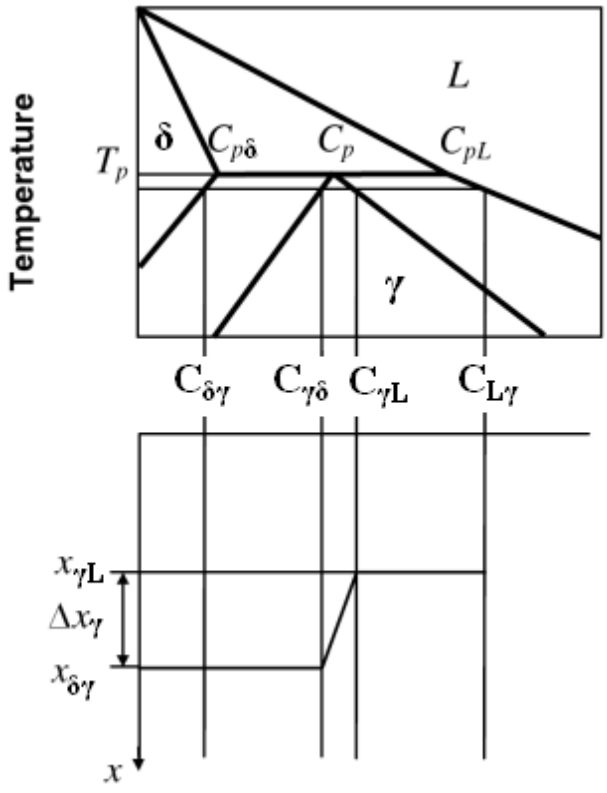

Fig. 1.21 Definition of quantities through Eq. 1.8 to 1.10 (Stefanescu, 2002)

contact and the liquid and δ-ferrite react to form austenite. This reaction is rapid, leading to the formation of a thin film of austenite along the liquid/δ-ferrite interface which separates the liquid and δ-ferrite. Once primary δ-ferrite is covered, peritectic transformation takes place by solid-state diffusion through the austenite phase. The austenite phase can also be formed by direct precipitation from the liquid, which does not depend on the presence of the primary phase (Ha and Hunt, 2000). In general, the amount of austenite formed is assumed to depend mainly on the peritectic transformation and direct solidification. This is because even though the peritectic reaction is rapid, the amount of austenite formed is a small fraction of the total.

The thickness of the peritectic layer increases with subsequent cooling by diffusion through the γ layer, precipitation of γ directly from the liquid and δ phase. Assuming isothermal transformation, the rate of peritectic transformation is controlled by the diffusion rate through the layer at a temperature just below peritectic temperature. The mass balance at the interface can be written as:

$$D_\gamma \left(\frac{\mathrm{d}C_\gamma}{\mathrm{d}x}\right)_{x=0} = -V \cdot \Delta C \tag{1.8}$$

Then, for the δ/γ interface and the γ/L interface we have, respectively:

$$D_\gamma \left.\frac{\partial C_\gamma}{\partial x}\right|_{x=\delta\gamma} = -\frac{\mathrm{d}x_{\delta\gamma}}{\mathrm{d}t}\left[C_{\delta\gamma} - C_{\gamma\delta}\right]$$

$$\text{and} \quad D_\gamma \left.\frac{\partial C_\gamma}{\partial x}\right|_{x=\gamma\mathrm{L}} = -\frac{\mathrm{d}x_{\gamma\mathrm{L}}}{\mathrm{d}t}\left[C_{\gamma\mathrm{L}} - C_{\mathrm{L}\gamma}\right] \tag{1.9}$$

where D_γ is the diffusion coefficient in the γ phase. All other terms are

defined in Fig. 1.22. Assuming that the concentration gradient through γ layer is constant, it can be expressed as:

$$\frac{\partial C_{\gamma}}{\partial x} = \frac{C_{\gamma \mathrm{L}} - C_{\gamma\delta}}{x_{\gamma \mathrm{L}} - x_{\gamma\delta}} = \frac{C_{\gamma \mathrm{L}} - C_{\gamma\delta}}{\Delta x}$$

Substituting in the above two equation and adding the equations leads to:

$$\frac{\mathrm{d}(\Delta x)}{\mathrm{d}t} = \frac{D_{\gamma}}{C_{\gamma\delta} - C_{\delta\gamma}} \frac{C_{\gamma \mathrm{L}} - C_{\gamma\delta}}{\Delta x} + \frac{D_{\gamma}}{C_{\gamma \mathrm{L}} - C_{\mathrm{L}\gamma}} \frac{C_{\gamma \mathrm{L}} - C_{\gamma\delta}}{\Delta x} = \frac{D_{\gamma}}{\Delta x} [\Omega_{\delta\gamma} + \Omega_{\gamma \mathrm{L}}]$$

where $\Omega_{\delta\gamma} = \frac{C_{\gamma \mathrm{L}} - C_{\gamma\delta}}{C_{\gamma\delta} - C_{\delta\gamma}}$ and $\Omega_{\gamma \mathrm{L}} = \frac{C_{\gamma \mathrm{L}} - C_{\gamma\delta}}{C_{\mathrm{L}\gamma} - C_{\gamma \mathrm{L}}}$

Integrating:

$$\Delta x_{\gamma} = \left[2 D_{\gamma} \left(\Omega_{\delta\gamma} + \Omega_{\gamma \mathrm{L}}\right) t\right]^{\frac{1}{2}} \qquad (1.10)$$

This equation shows that the growth rate increase with the difference between $C_{\gamma L}$ and $C_{\gamma\delta}$ which depends on the undercooling. Also, the growth rate is affected by diffusivity. For interstitially dissolved elements, the diffusion rates are high and in-situ observation in Fe-C systems demonstrated that the growth of the thickness of the γ phase follows a parabolic law which supports the opinion that the rate controlling phenomenon is carbon diffusion (Shibata *et al*., 2000).

On the other hand, the diffusion coefficient near the melting point is of the order of 10^{-13} m^2 s^{-1} for substitutional alloying elements in face-centered cubic metals. In such a case, the growth rate will be very slow and it requires quite long

time for peritectic transformation to proceed. In a normal casting process, the reaction rate will be so low that the amount of γ phase by the peritectic transformation will be negligible in comparison with the direct solidification of γ from the liquid.

Arai *et al.* (2005) observed peritectic solidification of Fe – Ni alloy with confocal scanning laser microscope (CSLM). The rate of the thickening of γ phase toward liquid is faster than toward δ phase and the author presumed that it is due to the slower diffusion of nickel in δ phase and the direct solidification of γ phase. The rate of direct solidification depends on the thermal field under which the solidification is being carried out, which means heat transfer controls the final stage of the peritectic solidification (McDonald and Sridhar, 2005, McDonald and Sridhar, 2003). In some cases, the microsegregation changes the solidification mode. The significant microsegregation of manganese in a hypo-peritectic steel promoted a change in the solidification mode, from a hypo-peritectic mode into a hyper-peritectic mode (Mondragón *et al*., 2008).

1.3. Scope of the Research

The as-cast microstructure of a δ-TRIP steel (Fe – 1.0Mn – 0.2Si – 3.6Al – 0.4C wt%) is shown in Fig. 1.22. The light part is ferrite, which inherited the dendrite structure of primary solid phase from the liquid. The structure indicates that primary δ-ferrite is retained to ambient temperature, as mentioned previous part. However, it is different from what the equilibrium phase fraction calculation shows, as presented in Fig. 1.23. The diagram is calculated using ThermoCalc (Version S) with the TCFE6 database. According to the diagram, δ phase is fully transformed into austenite at ~1300℃, which implies that the dendrite shape cannot remain at ambient temperature.

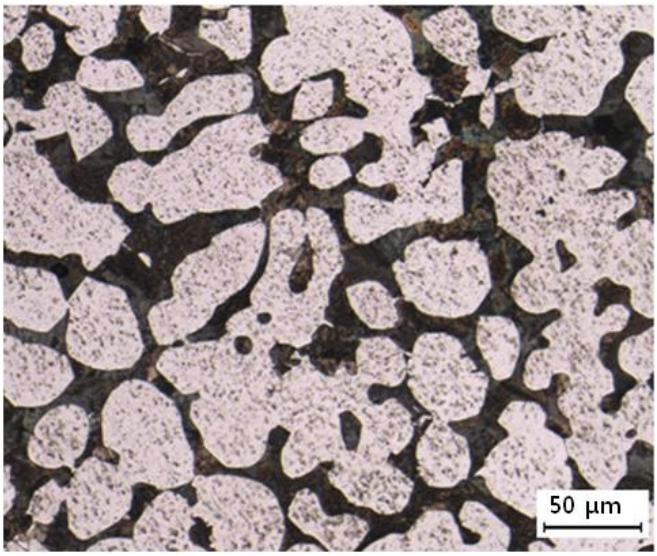

Fig. 1.22 As-cast microstructure of δ-TRIP steel

To confirm the validity of the calculation, a specimen of the same alloy was soaked at 1300 ℃ for 24 h and quenched to observe the microstructure (Fig. 1.24). The soaking time is determined based on the diffusion distance of manganese and aluminum in fcc phase of the alloy at 1300 ℃ for 24 h, using Eq. 1.11. The diffusivity of aluminum and manganese in fcc phase of the alloy at the temperature is around 4×10^{-13} m^2 s^{-2} and 7×10^{-14} m^2 s^{-2}, respectively. The diffusion distance for each calculated is 186 μm and 78 μm, which is greater than the secondary dendrite arm spacing measured from as-cast specimen. Thus it is considered sufficient to remove the microsegregation during solidification.

$$L = \sqrt{Dt} \tag{1.11}$$

where L is length in m, D is the diffusivity in m^2 s^{-1} and t is time in s.

The microstructure is fully martensitic which was austenite at high temperatures. This suggests that δ phase is possibly retained for kinetic reasons and the amount of residual δ phase could be varied according to the cooling condition. However, little has been studied about the kinetic effect although δ phase has great influence on the stability of austenite and heat affected zone during welding. This study, thus, will investigate the retention behavior depending on composition and cooling condition.

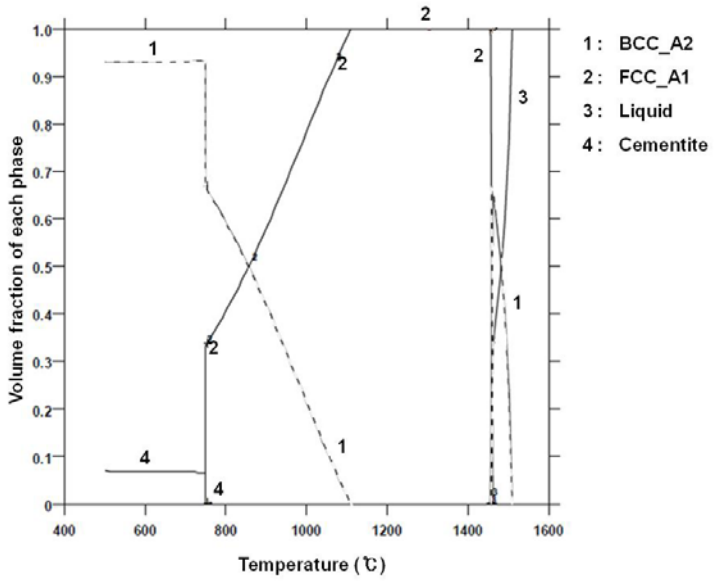

Fig. 1.23 Calculated equilibrium phase fraction of δ-TRIP steel. Dashed line represents ferrite.

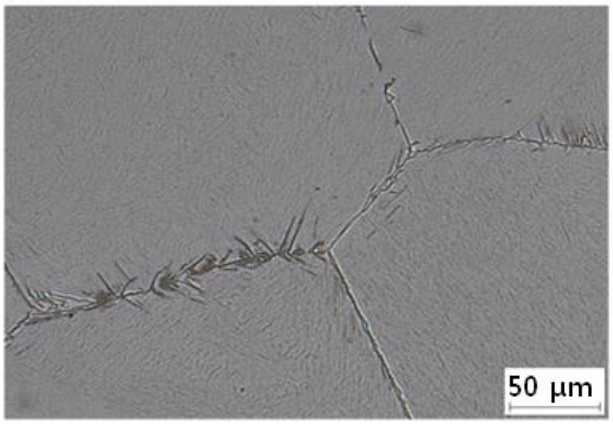

Fig. 1.24 The microstructure of the sample soaked at 1300℃ for 24 hours and quenched

2. Numerical Simulation

Since the cast structure is inconsistent with the achievement of equilibrium phase fractions, simulations have been conducted using DICTRA software to investigate the kinetic effect. The thermodynamic database TCFE6 and mobility database MOB2 (version 2.4) were used. The compositions of the alloys investigated are listed in Table 2.1 and the two alloys selected for simulation are alloys 3 and 5. Trace elements such as sulfur and nitrogen are excluded. The cell size set for the simulation is the approximate secondary dendrite arm spacing (SDAS) measured from as-cast specimens, i.e., 50 μm. The schematic geometry used in the simulation is illustrated in Fig. 2.1. Since the cooling rates of the ingots used are not known, 20 K s^{-1} was estimated using Eq. 2.1 which is obtained empirically using secondary dendrite arm spacing (SDAS) measured by several different researchers as a function of cooling rates and steel carbon content (Won and Thomas, 2001). For additional conditions, 2 K s^{-1} and 200 K s^{-1}

(wt%)

	C	Si	Mn	S	Al	N
Alloy 1	0.303	0.198	0.515	0.0030	3.45	0.0022
Alloy 3	0.310	0.208	0.511	0.0033	5.60	0.0036
Alloy 5	0.397	0.192	0.514	0.0012	3.53	0.0014
Alloy 7	0.393	0.188	0.501	-	5.57	-

Table 2.1 Chemical composition of the alloys

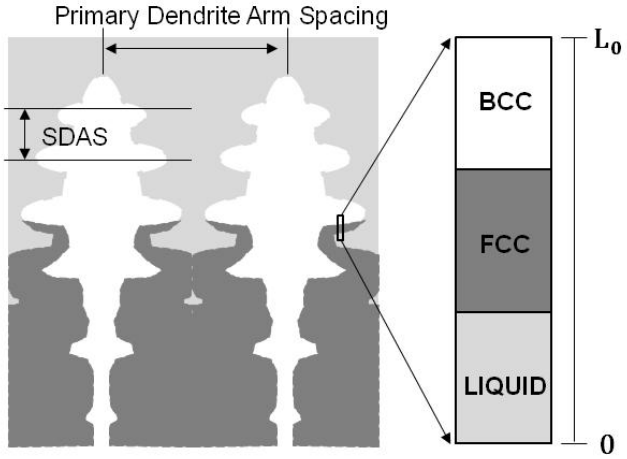

Fig. 2.1 Schematic geometry used in the kinetic simulation.
L_0: cell size for kinetic simulation, i.e. size of the unit segregation zone

are selected, expecting more δ phase under higher cooling rate.

$$\lambda_{\mathrm{SDAS}}(\mu\mathrm{m}) = (169.1 - 720.9 \cdot C_C) \cdot C_R^{-0.4935}$$

$$\text{for } 0 < C_C \leq 0.15$$

$$\lambda_{\mathrm{SDAS}}(\mu\mathrm{m}) = 143.9 \cdot C_R^{-0.3616} \cdot C_C^{0.5501-1.996\mathrm{C_C}}$$

$$\text{for } 0.15 < C_C \qquad (2.1)$$

where C_R is the cooling rate (K s^{-1}) and C_C is the carbon content (wt%)

The simulation results are indicated in Figs. 2.1 and 2.2, including equilibrium phase fraction diagrams for comparison. It is shown that the phase fractions deviate from equilibrium values as cooling rate increases but changes in the amount of δ phase are not as clear as expected. Instead, the γ to α phase transformation which occurs at lower temperatures seems to be stifled by higher

cooling rates.

The SDAS for 2 K s^{-1} and 200 K s^{-1} were estimated based on the Eq. 2.1, where higher cooling rate results in refinement. As shown in Figs. 2.3 and 2.4, the kinetic effect becomes more ambiguous if the variation in SDAS with cooling rate is taken into account even though it is more reasonable to modify the cell size according to the cooling condition. This is contradicts to the fact that a considerable amount of δ-ferrite exists in the as-cast specimen and implies that the simulation cannot fully accommodate kinetic effect.

For more accurate comparison, modified simulations which incorporated the actual cooling rate and SDAS from experimental data will be presented in the Experimental and Discussion part.

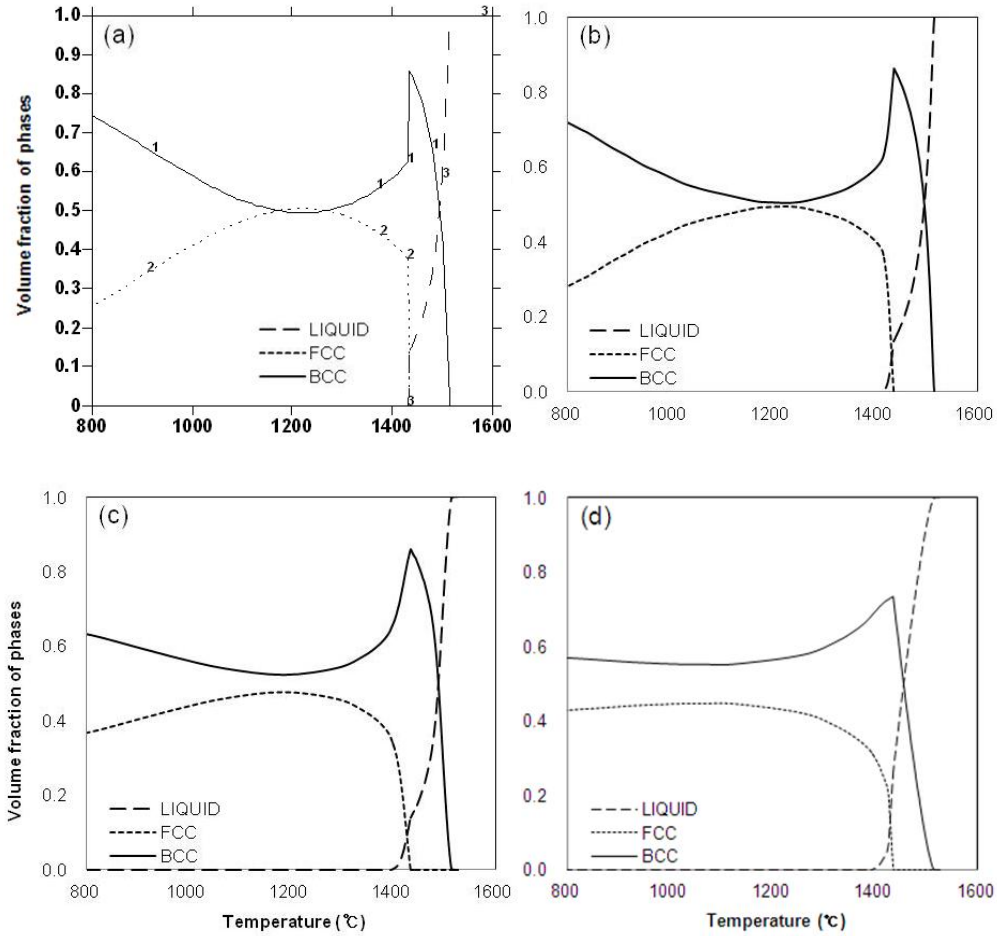

Fig. 2.1 Calculated phase fractions from ThermoCalc and DICTRA simulations for alloy 3, with a fixed cell size of 50 μm

(a) equilibrium phase fraction, (b) 2 K s^{-1}, (c) 20 K s^{-1} and (d) 200 K s^{-1}

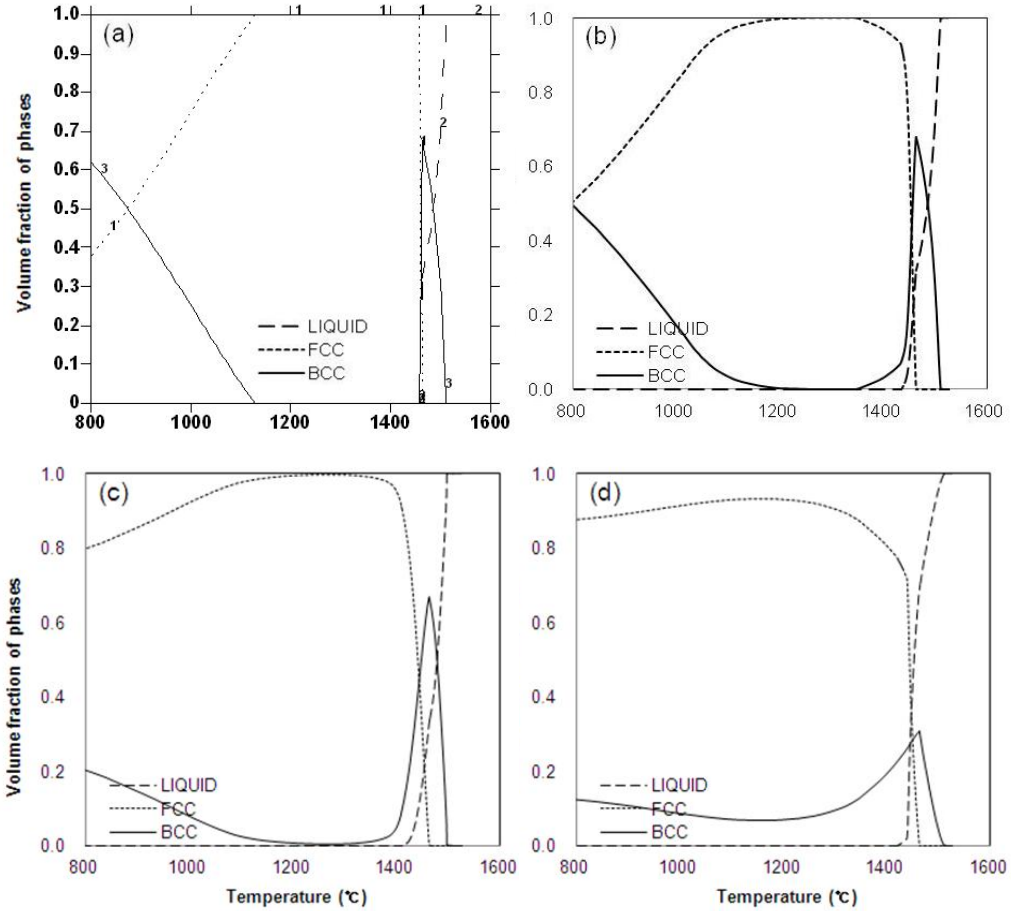

Fig. 2.2 Calculated phase fractions from ThermoCalc and DICTRA simulations for alloy 5, with a fixed cell size of 50 μm

(a) equilibrium phase fraction, (b) 2 K s^{-1}, (c) 20 K s^{-1} and (d) 200 K s^{-1}

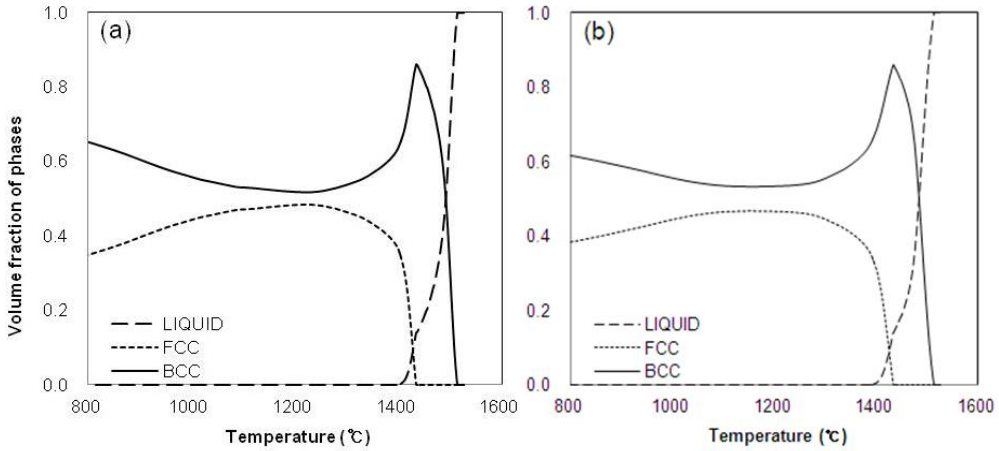

Fig. 2.3 Calculated phase fractions from DICTRA simulations for alloy 3, with modified cell sizes
(a) 2 K s^{-1} with 120 μm cell and (b) 200 K s^{-1} with 20 μm cell

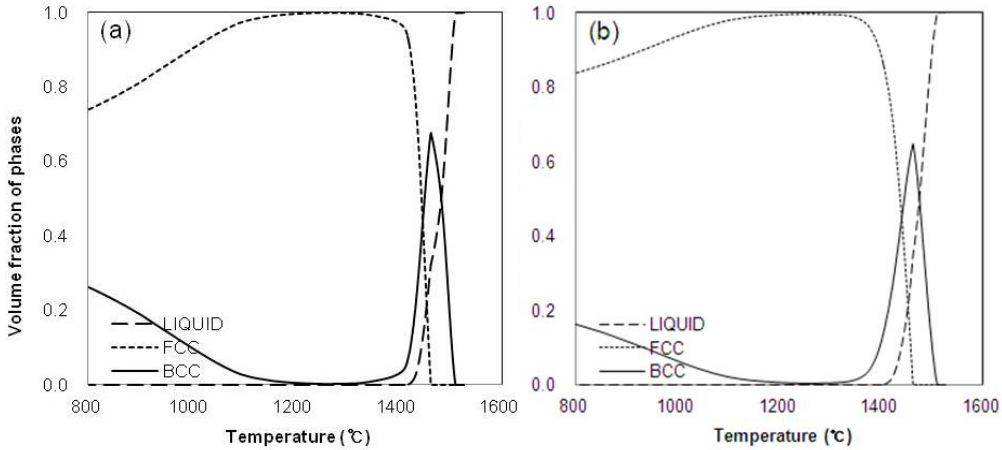

Fig. 2.4 Calculated phase fractions from DICTRA simulations for alloy 5, with modified cell sizes
(a) 2 K s^{-1} with 120 μm cell and (b) 200 K s^{-1} with 20 μm cell

3. Experiments

3.1. Experimental procedures

Four different alloys were fabricated in order to investigate the effect of aluminum and carbon content on the retention of δ-ferrite. The alloys were produced by POSCO and the manufacturing steps consisted of vacuum melting and casting to produce a 25 kg ingot for each alloy. The compositions are shown in Table 2.1.

To observe the changes in the phase fraction as a function of temperature under controlled conditions, a unidirectional solidification experiment was carried out using the apparatus shown in Fig. 3.1. The sample is contained in an alumina tube (298 mm in length, 10 mm outer diameter and 5.5 mm inner diameter), which is withdrawn downward from the induction furnace to the water cooling device below the mechanical part. The withdrawal rates were set to 30 mm m^{-1} and 300 mm m^{-1} corresponding to cooling rates which were measured to be 2.5 K s^{-1} and 8.1 K s^{-1} respectively. The temperature profile was recorded by a separate thermocouple for each withdrawal rate and the temperature history of the specimen was estimated based on those data.

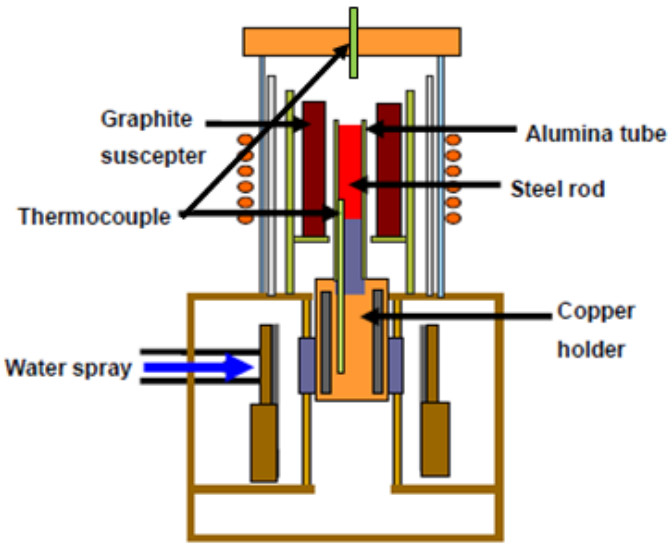

Fig. 3.1 Schematic illustration of a unidirectional solidification apparatus (Lee, 2008)

3.2. Microscopy

After the solidification experiments, the solidified specimens were cut along the longitudinal direction and microstructures of vertical section were observed. Optical microscopy samples were prepared using standard methods and etched in Oberhoffer's solution (0.5 g $SnCl_2$, 1 g $CuCl_2$, 30 g $FeCl_3$, 500 mL distilled water, 500 mL ethanol, 50 mL 32% HCl) for study using optical microscopy (Olympus: BX60). The volume fractions of ferrite were measured using point counting on optical micrographs.

In Fig. 3.2, the equilibrium phase fractions calculated from ThermoCalc software (version S) with TCFE6 database are presented. Fig. 3.3 shows the microstructures of four alloys quenched from similar temperature range (1120~1230 ℃) where according to the calculations, the austenite fraction becomes a maximum and then starts to decrease. The ferrite fractions of the alloys are not significantly different from each other with the exception of alloy 5 which has higher carbon and lower aluminum content. It is predictable that alloy 5 has lower ferrite fraction compared with other alloys from the calculated equilibrium phase diagram. A notable thing is that the skeletal dendrite of the remaining structure signifies that δ phase is not completely decomposed even for alloy 5, which is contrary to what the equilibrium phase fraction diagram suggests.

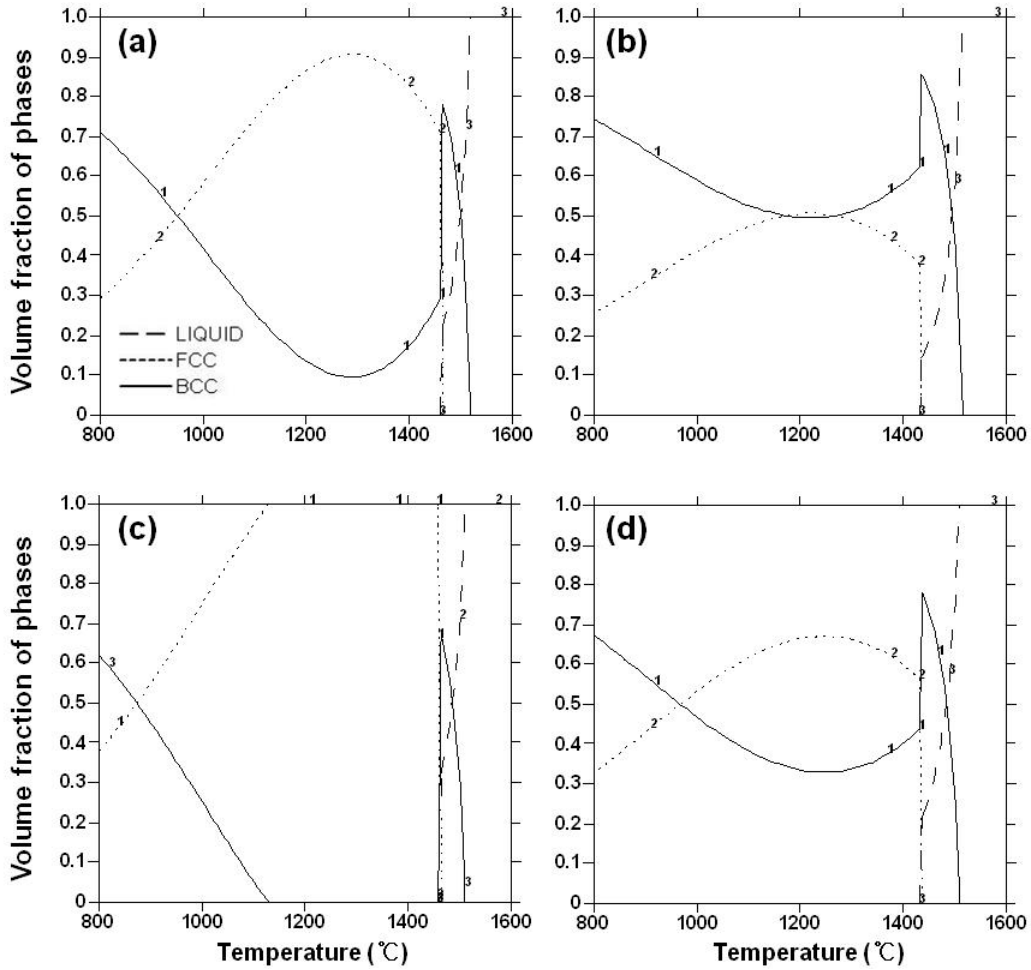

Fig. 3.2 Calculated equilibrium phase fractions for
(a) alloy 1, (b) alloy 3, (c) alloy 5 and (d) alloy 7

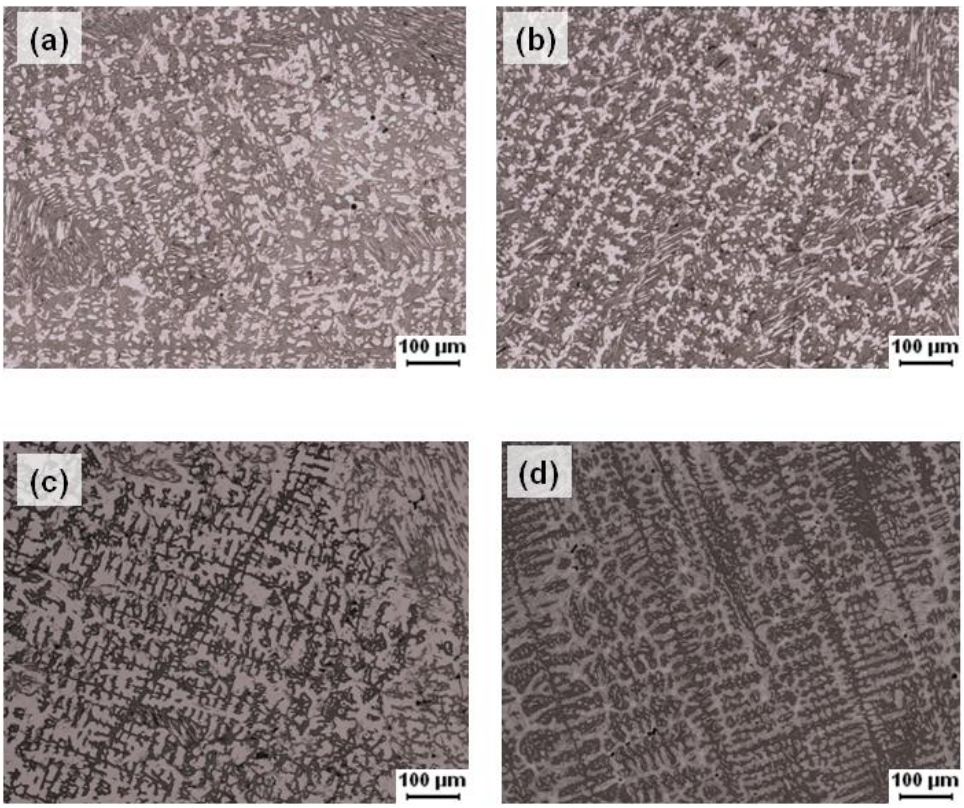

Fig. 3.3 The microstructures of specimens solidified with high cooling rate (8.1 K s^{-1})
(a) alloy 1, (b) alloy 3, (c) alloy 5 and (d) alloy 7

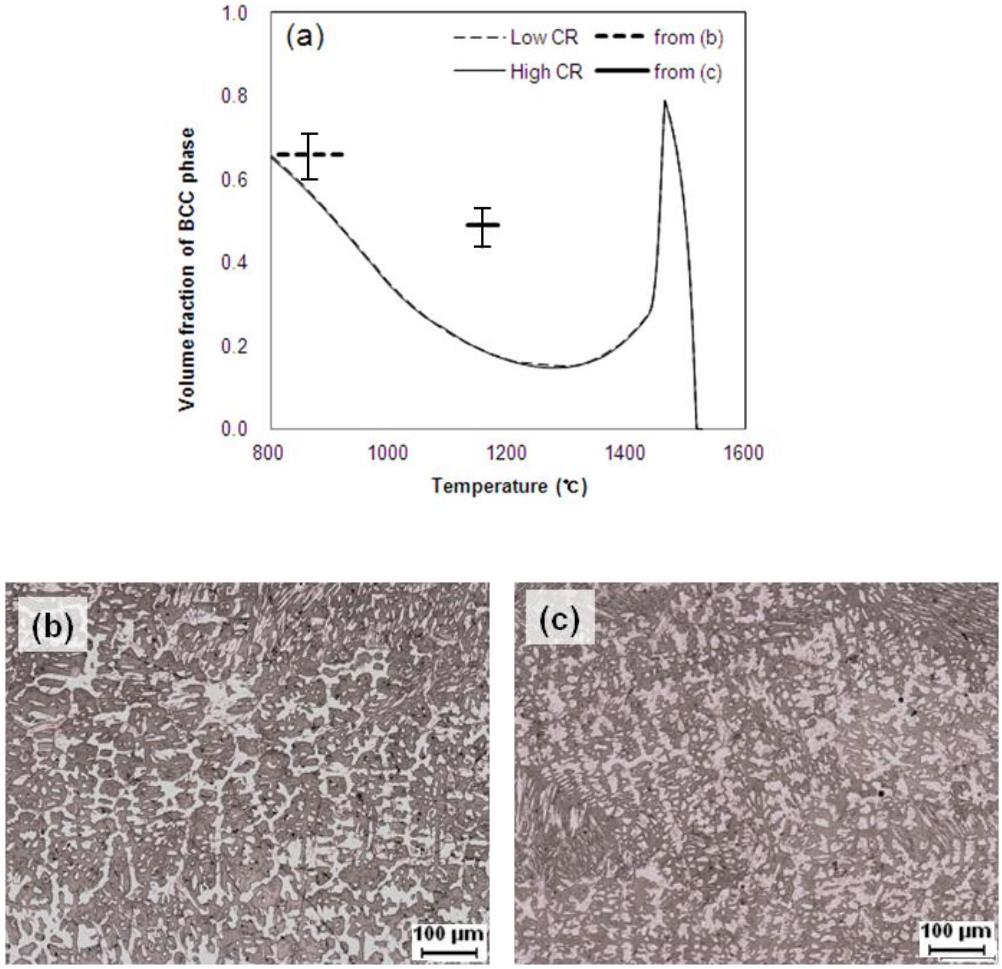

Fig. 3.4 (a) Calculated and measured ferrite fractions of alloy 1

(b) Alloy 1 quenched from 810~920 ˚C with low cooling rate (2.5 K s^{-1})

(c) Alloy 1 quenched from 1130~1180 ˚C with high cooling rate (8.1 K s^{-1})

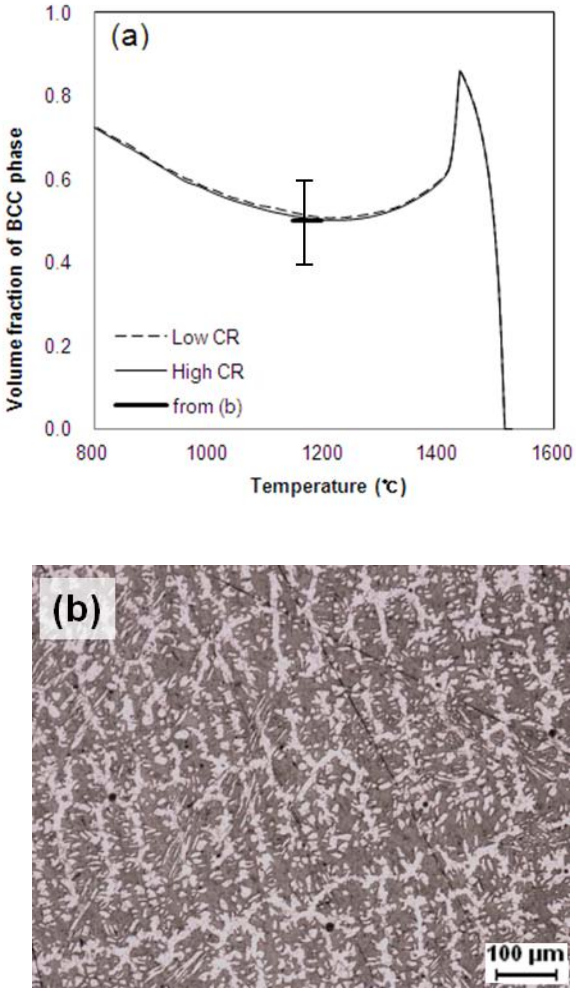

Fig. 3.5 (a) Calculated and measured ferrite fractions in alloy 3
(b) Alloy 3 quenched from 1145~1195 ˚C with high cooling rate (8.1 K s^{-1})

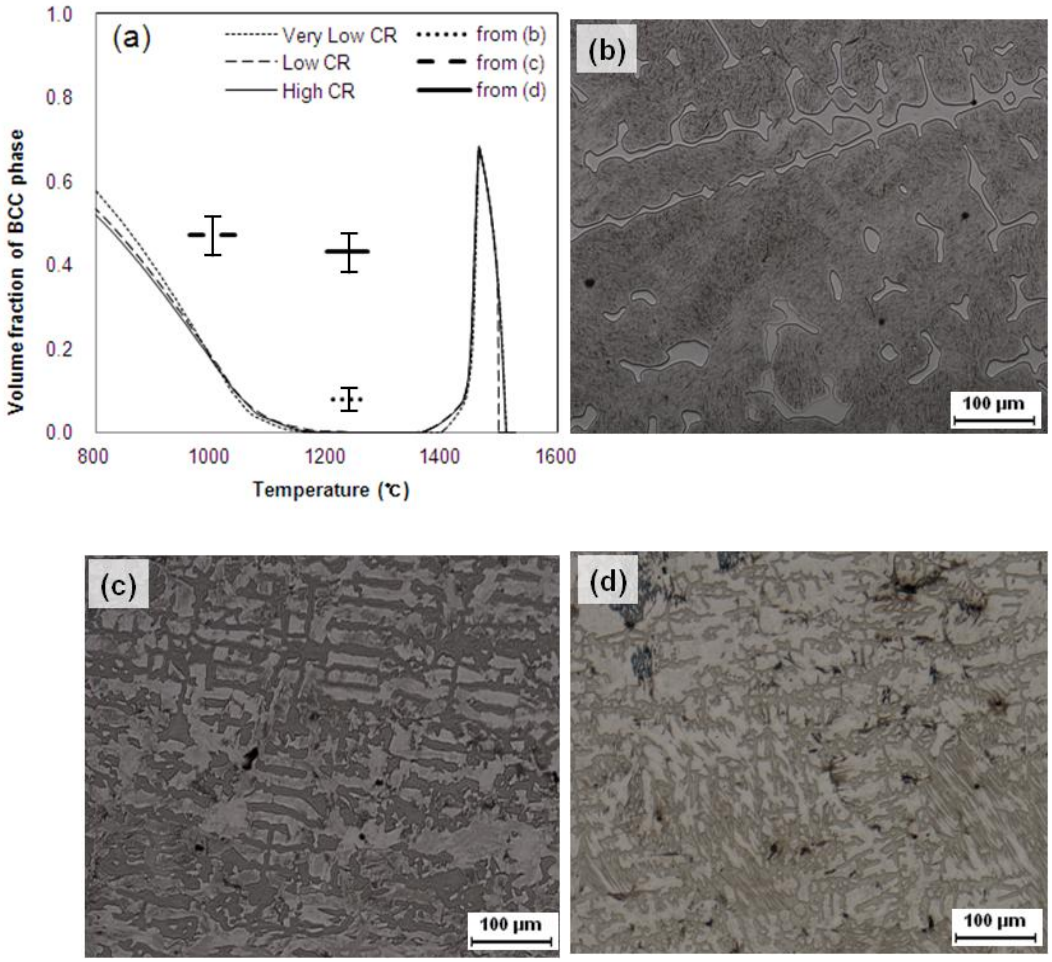

Fig. 3.6 (a) Calculated and measured ferrite fractions in alloy 5

(b) Alloy 5 quenched from 1210~1260 ˚C with very low cooling rate (0.4 K s^{-1})

(c) Alloy 5 quenched from 960~1050 ˚C with low cooling rate (2.5 K s^{-1})

(d) Alloy 5 quenched from 1200~1270 ˚C with high cooling rate (8.1 K s^{-1})

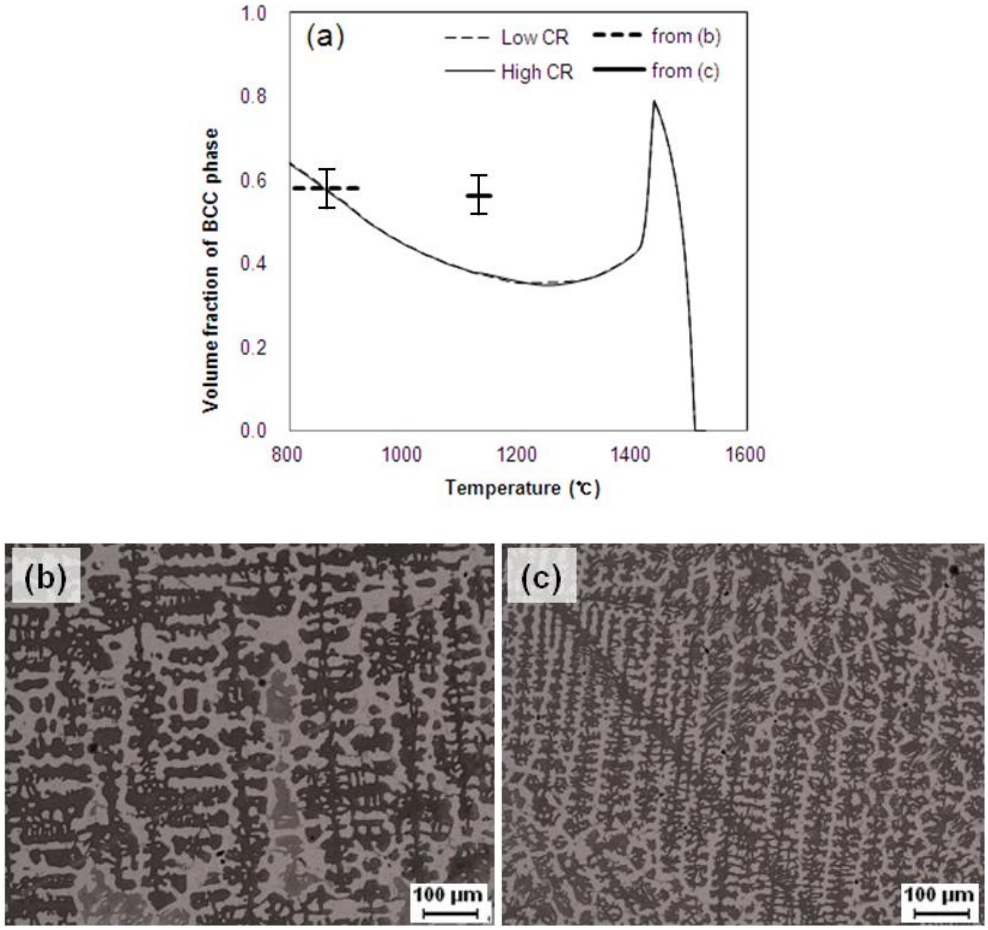

Fig. 3.7 (a) Calculated and measured ferrite fractions in alloy 7

(b) Alloy 7 quenched from 810~920 ˚C with low cooling rate (2.5 K s^{-1})

(c) Alloy 7 quenched from 1110~1150 ˚C with high cooling rate (8.1 K s^{-1})

From Figs. 3.4 to 3.7, measured ferrite fractions and predicted values are shown together for several temperatures. The curves shown in the figures are calculated BCC phase fractions from DICTRA simulations and the short bold lines indicate the fractions measured from the unidirectionally solidified specimens.

The DICTRA simulation was conducted in the same way as previous chapter but incorporated actual cooling rate and SDAS measured from the experimental result. The cell size was set to 36 μm for low cooling rate condition (2.5 K s^{-1}) and 21 μm for high cooling rate condition (8.1 K s^{-1}). The reason why each measured value appears as a line rather than a dot is that the temperature range from which the specimen quenched was estimated from the position of the specimen. An additional experiment and simulation with very slow cooling rate (0.4 K s^{-1}) was included for alloy 5, since the alloy showed the largest discrepancy between calculated equilibrium fraction and measured fractions.

In the case of alloy 1 with low cooling rate, the measured ferrite fraction is similar to the fraction from the simulation curve. However, the specimen with the greater cooling rate shows a higher ferrite fraction than the simulated result. For alloy 3, the ferrite fraction measured from high cooling rage specimen is in accord with the simulation curve although the observation in low cooling rate is absent due to a failed experiment. The measured ferrite fractions for alloy 5 as well as 7 are higher than those calculated, except the one quenched at around 800 ºC.

The ferrite fractions measured under 900 ºC generally correspond to the simulation curves. However, it is difficult to distinguish separate the kinetics of α-ferrite and δ-ferrite over such a temperature range. For specimens quenched from relatively high temperatures, the simulation curves always predicted lower fractions of ferrite than those measured, except alloy 3.

It is suggested that the discrepancy is related with the kinetics for the transformation of δ-ferrite into γ-austenite, considering that the primary phase is δ-ferrite when it starts to solidify. Especially for alloy 5, the kinetic simulations for different cooling rates show nearly similar curves while the ferrite fraction measured from specimens obviously increases with the cooling rate. In fact, there is little difference between the DICTRA simulation curves and the equilibrium phase fractions calculated from ThermoCalc. The reason why there is an agreement between simulation result and measured value for alloy 3 is presumed to be that its equilibrium ferrite fraction is very high due to its lower carbon and higher aluminum content, which in turn makes the kinetic effect insignificant compared with other alloys.

4. Discussion

There are some discrepancies between observed quantity of ferrite and that predicted, as presented in the preceding chapter. The non-equilibrium microstructures of δ-TRIP steel have previously been investigated by Yi *et al*. (2010). The microscopic features of alloys designed on the basis of equilibrium to contain substantial amount of δ-ferrite, revealed much reduced fractions of δ-ferrite in the solidified condition. According to the authors, the feature responsible for the diminished quantities of δ-ferrite is that the solid-state transformation of δ-ferrite into austenite occurs without the required partitioning of solutes, i.e. by a process which may not be far from paraequilibrium. However, such interpretation should be modified given that the updated thermodynamic database, TCFE6, indicates totally different phase fraction evolutions. It is noted that the TCFE6 database is more accurate for the prediction of the relative stabilities of austenite and ferrite in aluminum and copper-rich alloys, in the ThermoCalc database description. This improvement can also be verified with the alloys used in this study, by soaking the specimens at 1300 ºC for 24 h so as to achieve microstructures close to that of equilibrium. The temperature was selected in order to observe the point at which the ferrite fraction becomes minimized. The soaking time is determined based on the diffusion distance calculation of manganese and aluminum in steel, as discussed in the Chapter 1.3. The microstructures as well as ferrite fractions of the as-cast and soaked

specimens are shown in Figs. 4.1 and 4.2, respectively. The equilibrium phase diagrams using ThermoCalc software with TCFE6 database were presented in the preceding chapter (Fig. 3.2) and the same diagrams with previous version of database, TCFE4, are plotted in Fig. 4.3. These figures suggest that TCFE6 database gives more reliable results than TCFE4 and the ferrite fractions in as-cast condition are not reduced amount but increased amount. Moreover, the distribution of each element using electron microprobe analysis (EPMA) indicates that aluminum, a substitutional alloying element, does partition into δ-ferrite as shown in Fig. 4.4.

In short, the main drawback is not related with thermodynamic database but the way to deal with the kinetics. The microstructures showed larger amounts of dendritic δ-ferrite than the minimum amount of ferrite phase shown in equilibrium phase fraction diagram, which implies that the δ to γ transformation rate is much lower than expected. The decrease in δ-ferrite fraction is especially rapid in the region where liquid, δ and γ phases coexist.

Several reasons can be considered to explain the overestimation of transformation kinetics. Some of the reasons are attributed to the accuracy of diffusivity or dimensions set in kinetic simulation, while others are associated with the relative consumption rate of δ and liquid phase when the austenite phase grows at the interface between the two phases.

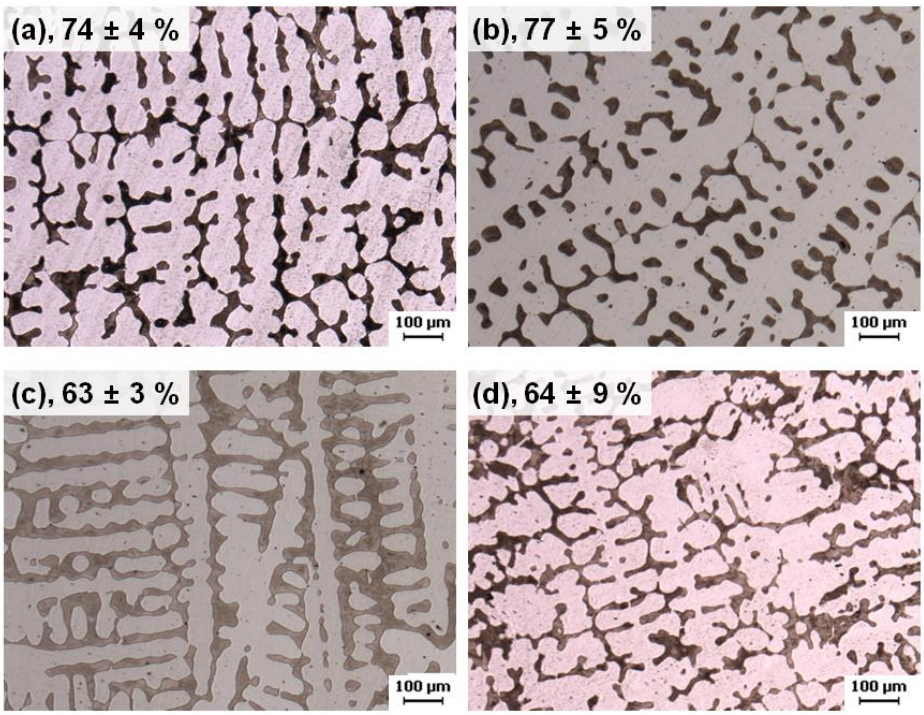

Fig. 4.1 As-cast microstructures and ferrite volume percents of (a) alloy 1, (b) alloy 3, (c) alloy 5, and (d) alloy 7

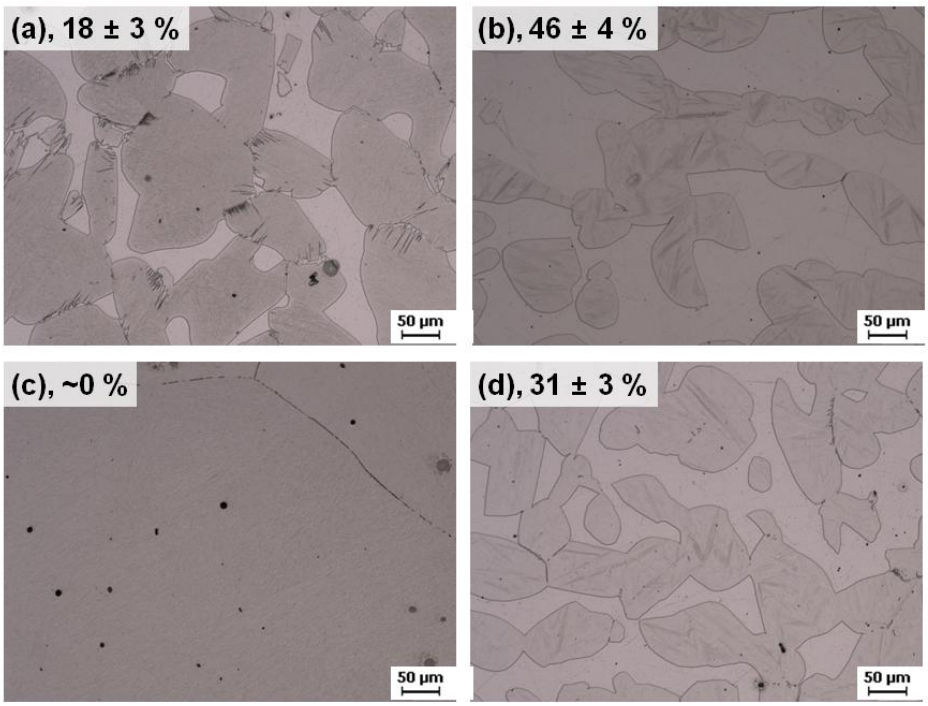

Fig. 4.2 The microstructures and ferrite volume percents of the specimens soaked at 1300 ºC for 24 h and quenched
(a) alloy 1, (b) alloy 3, (c) alloy 5, and (d) alloy 7

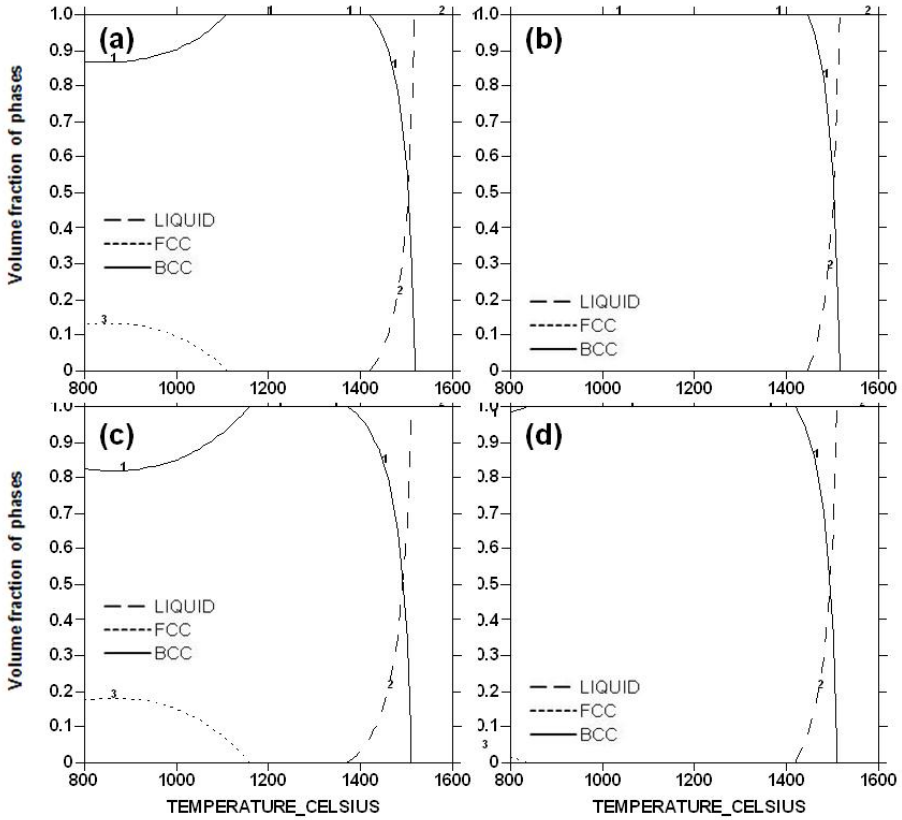

Fig. 4.3 Equilibrium phase fractions from the ThermoCalc calculation with TCFE4 database

(a) alloy 1, (b) alloy 3, (c) alloy 5, and (d) alloy 7

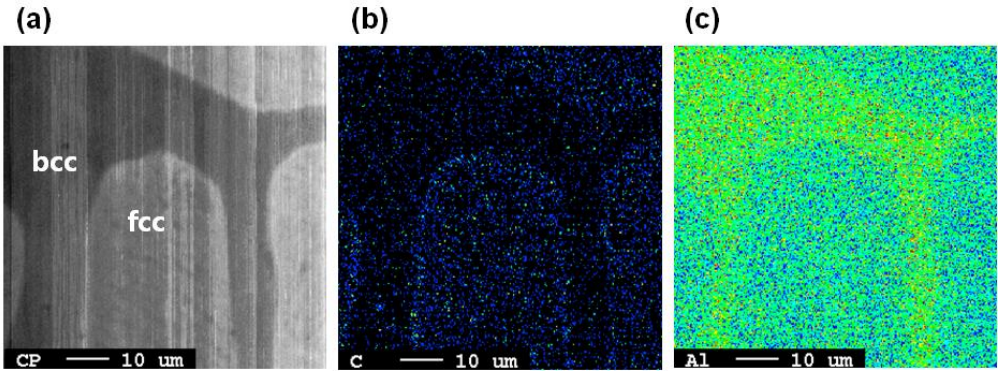

Fig. 4.4 EPMA images of dendritic microstructures at around 1280 ˚C of alloy 5; (b) and (c) indicate carbon and aluminum, respectively.

4.1 Solute Movements

One probable explanation of the discrepancy between the actual and simulated transformation kinetics may come from the overestimation of diffusivities in δ and γ phases in the mobility database. It can affect the transformation kinetics in two ways. One is the microsegregation level which depends on the degree of back-diffusion of solutes in solid phases, i.e. δ-ferrite in this case. The difference in solute concentration between liquid and δ-ferrite will be reduced if diffusivity of solutes in the solid phase is overestimated, which in turn creates a more favorable environment for austenite to grow since less solute diffusion is required. The other way is the solid state transformation kinetics. Overestimated diffusivities, of course, will result in higher δ→γ transformation rate. However, if the inaccurate diffusivity were the reason of the inconsistency of kinetic simulations with experimental observation, the dependence of cooling rate and the amount of remaining δ-ferrite should have been revealed even if the ferrite fraction in absolute terms may not be correct. Furthermore, the microsegregation is nearly constant over wide ranges of cooling rates owing to the coarsening of dendrite structure (Flemings, 1974b). The dendrite arm spacing varies with cooling rate and this variation is such that the extent of diffusion occurring during and after solidification is nearly constant. The specimens solidified with different cooling rates also indicate similar levels of segregation as indicated in Fig. 4.5. Thus, it is necessary to consider other factors.

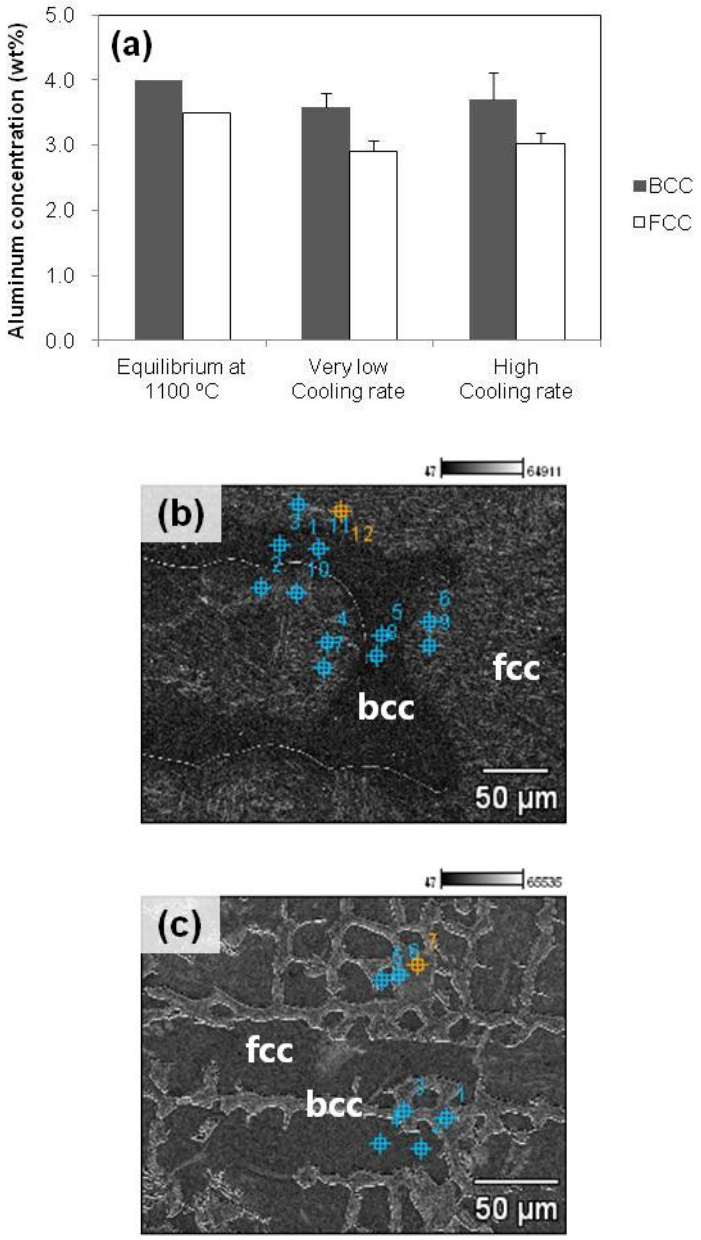

Fig. 4.5 Energy dispersive X-ray microanalysis result for alloy 5

(CARL Zeiss ULTRA 55 FE-SEM)

(a) average aluminum concentration, (b) cooling rate 0.4 K s^{-1} and (c) 8.1 K s^{-1}

Meanwhile, the austenite grows into both liquid and δ phases in the course of peritectic transformation. It raises a question about the relative moving velocity of liquid/γ interface and δ/γ interface, and also about the estimation of liquid diffusivity.

In the previous kinetic simulation done, the austenite phase grows more into δ-ferrite as shown in Fig. 4.6. However, it is reported that there is a transition point where the liquid/γ interface propagates faster than γ/δ interface as the cooling rate increased (Phelan *et al.*, 2006), from observations using high-temperature laser scanning confocal microscopy as well as the results from phase field modeling. The γ/δ interface propagates at a higher velocity than liquid/γ interface at low cooling rates as the finding of previous researchers. However, earlier modeling work in which complete diffusion in the liquid phase was assumed could not fully describe the inversion at high cooling rates. According to the authors, the inversion is attributed to the development of a steep concentration gradient in the liquid at a cooling rate of 1.7 K s^{-1} which leads to the increase in the flux of carbon from the austenite to the liquid phase, as shown in Fig. 4.7. Although the results were obtained from Fe – 0.18C wt% alloy which is significantly different from the alloy used in this study, it is worth paying attention since there will remain more δ-ferrite if austenite grows faster into the liquid phase. In addition, DICTRA software also considers diffusion in the liquid phase very fast and the diffusion coefficient in liquid is regarded as a constant, i.e. 10^{-9} m^2 s^{-1} under the conditions used in this study.

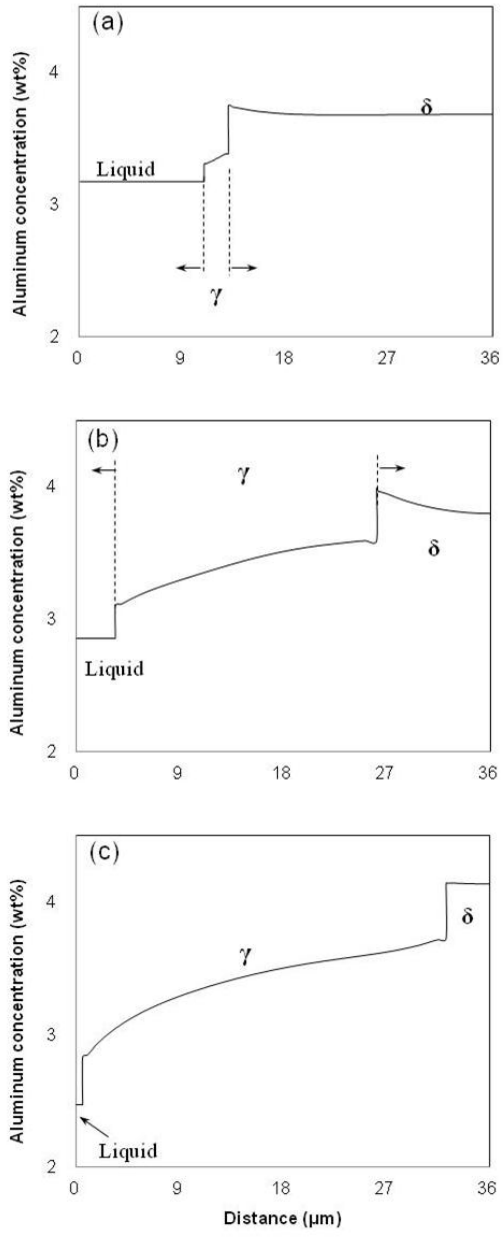

Fig. 4.6 Aluminum concentration profiles of alloy 5 (2.5 K s^{-1}, 36 μm cell) (a) 1462 ºC, (b) 1452 ºC and (c) 1442 ºC

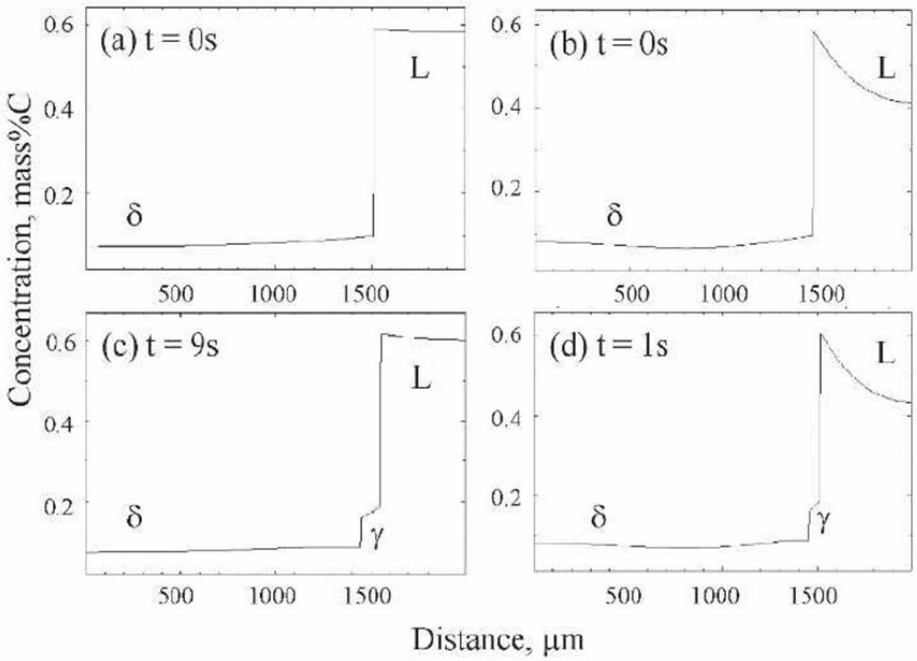

Fig. 4.7 Comparison of simulation solute profiles for cooling rates of (a) and (c) 0.17 K s^{-1} and (b) and (d) 1.7 K s^{-1}, in an Fe-0.18C wt% alloy; t=0 refers to the initiation of the peritectic phase transition (Phelan *et al*., 2006)

In order to examine the effect of modified diffusivity of solutes in liquid phase, 100 times lower than the default diffusivity was assumed and applied for the simulation shown in Fig. 4.8. The reason for 100 times lower value was set is that the diffusivity in the bcc phase will exceed that in the liquid phase if further reduction is applied. It turned out that a slight concentration gradient formed in the liquid phase but there is little difference in the phase fraction. This is probably due to the different alloy composition, since substitutional solutes such as aluminum lead to much slower diffusion in the austenite which controls the

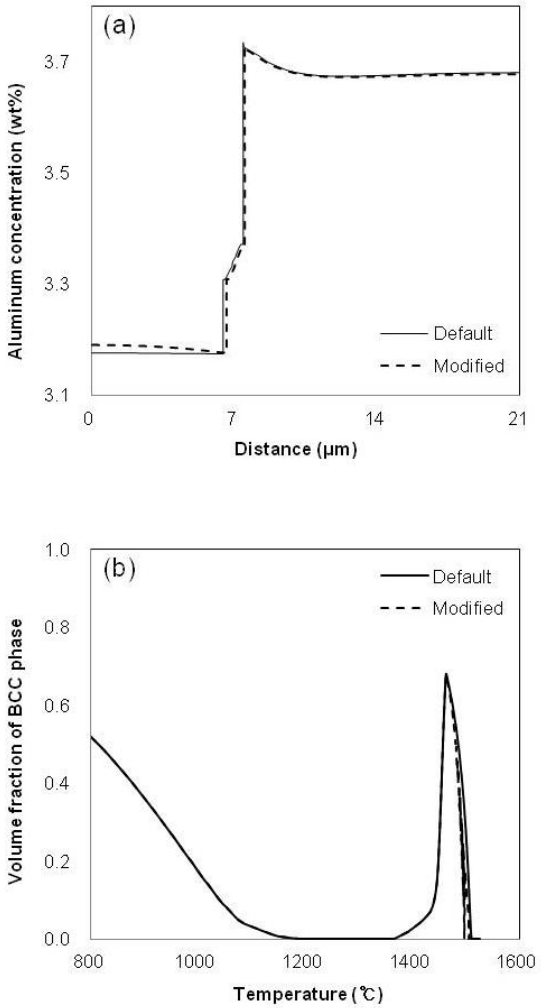

Fig. 4.8 Comparison of simulation results between default and 100 times slower diffusion coefficient of solutes in the liquid phase for alloy 5 (8.1 K s^{-1})
(a) aluminum profile and (b) ferrite fraction versus temperature

overall kinetics. It is also confirmed by the previous research which states that the modification of diffusion coefficients by 0.1 ~ 5 times has a negligible influence on the kinetic simulation results in type 304 stainless steel (Lee, 1998).

Another factor is the dimension (cell size) set for the simulation, since mass transfer among the phases is less effective when the cell size is large due to the large diffusion length. Indeed, it is reported that the interdendritic phosphorus concentration increases with an increase in the size of unit segregation zone set for DICTRA simulation, in the study on the effect of phosphorus addition on the phase transformation behavior of low-carbon steels (Kim *et al.*, 2006). Another modeling study on the microstructure of welds with high aluminum concentration (~1.7 wt%) successfully evaluated the deviation from the equilibrium ferrite fraction with different cooling rates, which indicates a large amount of retained δ-ferrite (BABU *et al.*, 2001). However, the dendrite arm spacing they assumed for calculations, 200 μm, was a few times larger than the secondary dendrite arm spacing which can be estimated from the micrograph they presented. The changes in dendrite arm spacing with different cooling rate were not considered either. Actually, considering the evolution of dendrite structure and the characteristics of peritectic transformation, the cooling rate may have little impact on the amount of austenite phase formed by peritectic transformation, i.e., the solid state transformation whose rate is controlled by the diffusion of solutes in the austenite phase. It is because a higher cooling rate leads to finer dendrite structure which provides more nucleation sites for austenite but at the same time

less time to proceed with the peritectic transformation.

To sum up, it is necessary to explore factors other than the growth aspect related with diffusion of solutes.

4.2. Partition Characteristics

As mentioned before, the rate of decomposition of δ phase and formation of γ phase is very rapid in the three-phase region where liquid, γ and δ phase coexist. Then the slope becomes less steep after most of the liquid is consumed. It suggests that the kinetics of peritectic transformation in the three-phase region is critical to the amount of δ-ferrite retained. In the case of substitutional alloying elements, the peritectic transformation rate will be so low that a considerable amount of austenite phase was formed by the direct precipitation from the liquid (Stefanescu, 2002). Direct solidification of austenite from the liquid phase, which is not included in DICTRA simulation, should be taken into account since the alloys used in this study contains a relatively high concentration of aluminum.

In general, the solutes are partitioned into the liquid phase from the growing solid during solidification. However, the reverse is true for some elements such as chromium whose partition coefficient is larger than unity. Aluminum also partitions into the solid phase when solidified, thus the liquid phase becomes aluminum-depleted during the solidification of δ-ferrite which consequently promotes the direct solidification of austenite from liquid phase since it does not require the diffusion of solutes across austenite from ferrite. The chemical composition of liquid phase after incomplete peritectic transformation and further cooling is actually in the liquid + γ region, as indicated in Fig. 4.9. The solidification mode change due to microsegregation was previously reported also

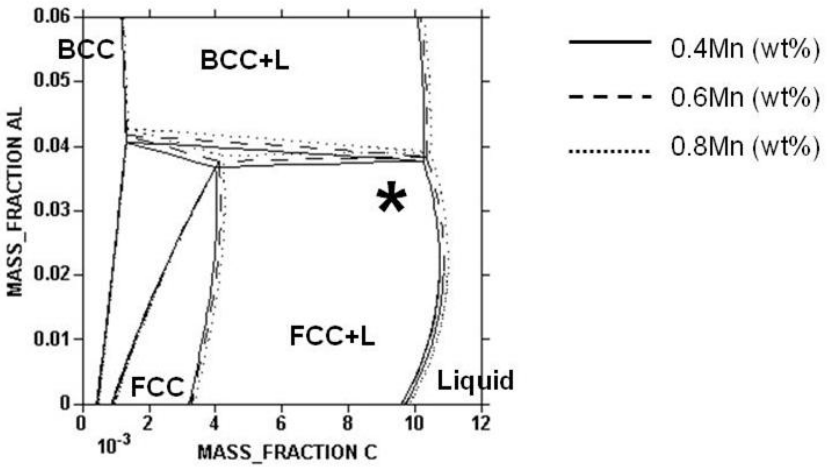

Fig. 4.9 Calculated isothermal section (1462 ºC) using ThermoCalc
The composition of segregated liquid is marked on the diagram (*).

by Mondragón *et al*. (2008). Direct solidification proceeds at much higher rate than peritectic transformation which involves the decomposition of δ-ferrite, thus it can explain that considerable amount of δ-ferrite remains at the stage of the completion of solidification, as illustrated in Fig. 4.10. If the cooling rate is slow enough to allow peritectic transformation, the ratio of dendrite arm thickness to dendrite arm spacing will become thinner as Figs. 4.10a and c. Otherwise, austenite grows faster toward liquid phase due to the direct solidification, which in turn leads to higher ratio of dendrite thickness as Figs. 4.10b and d.

It is the characteristics of partition of aluminum that emphasizes the role of direct solidification into γ in δ-TRIP steels compared with other alloys. Several

studies on the kinetic simulation of peritectic solidification with type 304 stainless steels, for example, obtained results with comparable amount of δ-ferrite (Lee, 1998, Hillert and Larsölund, 1999, Lee *et al.*, 1998). In such case, the direct solidification of austenite is less likely to occur since the chemical composition of the liquid phase is closer to that of ferrite as shown in Fig. 4.11. Thus DICTRA simulations could successfully describe the kinetics of phase transformation.

In conclusion, it is difficult to quantitatively predict the amount of δ-ferrite at ambient temperature with kinetic simulation using DICTRA although the retention behavior basically comes from the chemical segregation. Nevertheless, it is envisaged that the amount of retained δ-ferrite is analogous to that at the temperature where the austenite starts to form during solidification, under high cooling rates such as small ingot casting used in this study. This means the amount of austenite formed by peritectic transformation, accompanying the decomposition of δ-ferrite, is negligible. On the other hand, it will approach the equilibrium phase fraction under very slow cooling rates, as shown in Fig. 3.6 and verified with the specimens soaked at 1300 ℃ for 24 h. Fig. 4.12 compares the ferrite fraction measured from as-cast specimens as well as soaked specimens versus estimated fractions from DICTRA simulations and equilibrium phase fraction diagrams, including additional specimens with different chemical composition (Table 4.1).

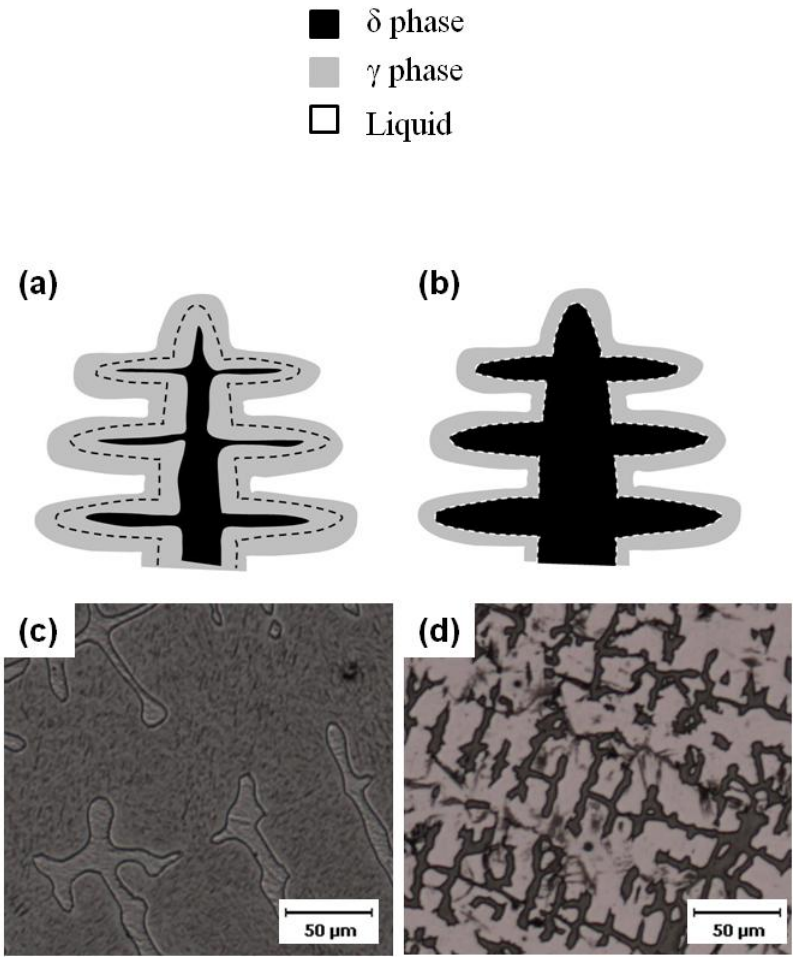

Fig. 4.10 Schematic illustration of dendrite; dashed line is liquid/δ interface where γ phase starts to form.

(a) γ phase grows toward both direction by peritectic transformation,

(b) most of γ phase formed by direct solidification, leaving δ phase untransformed,

(c) dendrite arm structure of very low cooling rate specimen (0.4 K s^{-1}, alloy 5) and (d) high cooling rate specimen (8.1 K s^{-1}, alloy 5)

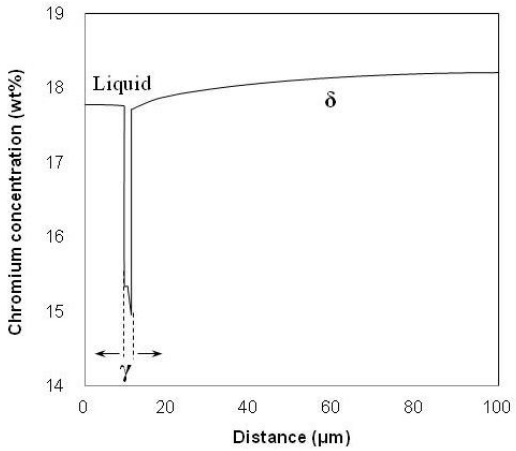

Fig. 4.11 Chromium concentration profiles of type 304 stainless steel (Fe – 18Ni – 8Cr wt%) at 1455 ºC

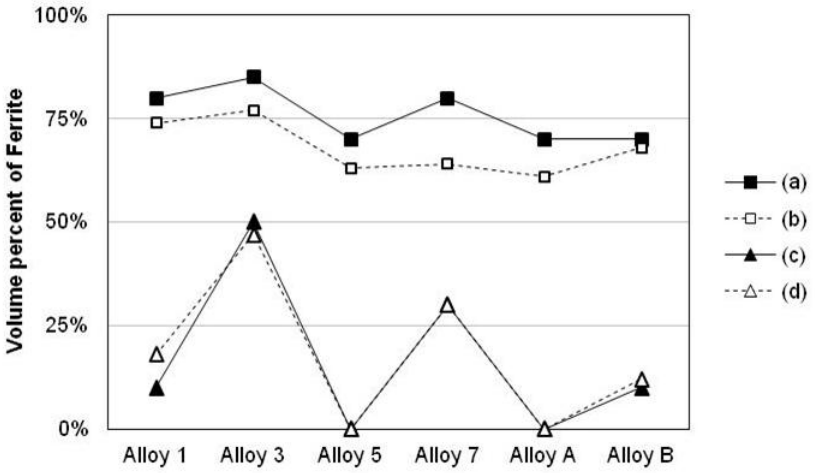

Fig. 4.12 The estimation of the volume fractions of ferrite

(a) calculated value; the maximum δ-ferrite fraction during solidification

(b) measured from the as-cast specimens

(c) calculated value at around 1300 ℃

(d) measured from the specimens soaked at 1300 ℃ for 24 h

(wt%)

	C	Si	Mn	S	Al	N
Alloy A	0.40	0.19	1.01	-	3.59	-
Alloy B	0.40	0.18	0.50	-	4.39	-

Table 4.1 Chemical composition of the additional alloys in Fig. 4.12

5. Conclusion

The solidification of δ-TRIP steel has been studied, which is characterized by the retention of δ-ferrite. Since the retention of δ-ferrite is attributed to kinetic effects, DICTRA simulation has been conducted. However, there is discrepancy in the room temperature δ-ferrite fraction between simulated value and experimentally measured one. It is suggested that the discrepancy mostly comes from the three-phase region where most of δ-phase disappears at rapid rate in the simulation while the experimental results indicate that considerable amount of δ-phase is retained. In a real solidification situation, the amount of γ phase formed by peritectic transformation would be very small, especially when involved with substitutional alloying elements as well as high cooling rate. In addition, the chemical composition of the liquid is in favorable condition to transform into γ phase due to segregation. Thus γ phase should grow into the liquid by direct solidification during peritectic solidification.

It should be pointed out that the thermodynamic database TCFE6 correctly reproduces the measured equilibrium fractions of δ-ferrite at 1300 ˚C for the alloys used in this study, which the previous database TCFE4 does not. The cast microstructures showed diminished quantities of δ-ferrite compared with those calculated using TCFE4 database, which was difficult to be explained without introducing para-equilibrium mode. However, the amount of δ-ferrite is actually greater than those calculated using TCFE6 database which is proved to be more

reliable. It leads to more straightforward explanation: the retention of δ-ferrite is attributed to kinetic effect and the deviation from the equilibrium phase fraction becomes greater as cooling rate increases.

The attempt to estimate the amount of δ-ferrite at room temperature according to the cooling rates has not been successful. Even so, it is predictable that the amount of δ-ferrite is close to the maximum amount of primary δ phase estimated by Thermo-Calc calculation under high cooling rates such as small ingot casting.

From a practical point of view, the following two can be pointed out to design δ-TRIP alloys, in which the retention of δ-ferrite plays a key role, using commercial thermodynamic software such as ThermoCalc. First, the maximum amount of δ-ferrite in phase fraction diagram can be a guide when one can obtain sufficient high cooling rate in casting process, e.g. strip casting. In this case, proper conditions for the successive process such as reheating and hot-rolling as well as casting should be set in order to maintain δ-ferrite throughout the process. The other is to design an alloy containing sufficient contents of aluminum so that the δ-ferrite does not disappear at any conditions, which can be predicted from the minimum amount of δ-ferrite in phase fraction diagram. This is necessary since the cooling rate may not be fast enough for normal continuous casting of large slabs, especially for the central part.

References

ARAI, Y., EMI, T., FREDRIKSSON, H. & SHIBATA, H. 2005. In-Situ observed dynamics of peritectic solidification and δ/γ transformation of Fe-3 to 5 At. pct Ni alloys. *Metallurgical and Materials Transactions A,* 36**,** 3065-3074.

BABU, S. S., DAVID, S. A. & QUINTANA, M. A. 2001. Modeling Microstructure Development in Self-Shielded Flux Cored Arc Welds. *Welding Journal,* 80**,** 91s-97s.

BHADESHIA, H. K. D. H. 2001. *Bainite in Steels,* UK, The University Press, Cambridge.

BHADESHIA, H. K. D. H. & HONEYCOMBE, R. W. K. 2006. *Steels: Microstructure and Properties,* UK, Elsevier.

BOWER, T. F., BRODY, H. D. & FLEMINGS, M. C. 1966. Measurements of Solute Redistribution in Dendritic Solidification. *Transaction of the Metallurgical Society of AIME,* 236**,** 624-633.

BRODY, H. D. & FLEMINGS, M. C. 1966. Solute Redistribution in Dendritic Solidification. *AIME MET SOC TRANS,* 236**,** 615-624.

CHATTERJEE, S., MURUGANANTH, M. & BHADESHIA, H. K. D. H. 2007. δ TRIP steel. *Materials Science and Technology,* 23**,** 819-827.

CHEN, Y., CHEN, X., YUAN, Z. X., XU, B. F., GUO, A. M., LI, P. H. & PU, S. K. 2002. Effects of Carbon Content and Rolling Processing on Retained Austenite for Hot-Rolled TRIP Steels. *ACTA METALLURGICA SINICA,* 15**,** 439-447.

CLYNE, T. & KURZ, W. 1981. Solute redistribution during solidification with rapid solid state diffusion. *Metallurgical and Materials Transactions A,* 12**,** 965-971.

DAS, A., MANNA, I. & PABI, S. K. 1999. A numerical model of peritectic transformation. *Acta Materialia,* 47**,** 1379-1388.

DE COOMAN, B. C., SPEER, J. G., PYSHMINTSEV, I. Y. & YOSHINAGA, N. 2007. *Materials design: the key to modern steel products*, GRIPS media.

FLEMINGS, M. 1974a. Solidification processing. *Metallurgical and Materials Transactions B,* 5**,** 2121-2134.

FLEMINGS, M. C. 1974b. *Solidification Processing,* New York, McGraw-Hill.

GHOSH, C., HALDAR, A., GHOSH, P. & RAY, R. K. 2008. Microstructure, Texture, Grain Boundary Characteristics and Mechanical Properties of a Cold Rolled and Annealed Martensitic Steel. *ISIJ International,* 48**,** 1626-1634.

HA, H. & HUNT, J. 2000. A numerical and experimental study of the rate of transformation in three directionally grown peritectic systems. *Metallurgical and Materials Transactions A,* 31**,** 29-34.

HASHIMOTO, S., IKEDA, S., SUGIMOTO, K.-I. & MIYAKE, S. 2004. Effects of Nb and Mo Addition to 0.2%C - 1.5%Si - 1.5%Mn Steel on Mechanical Properties of Hot Rolled TRIP-aided Steel Sheets. *ISIJ International,* 44**,** 1590-1598.

HILLERT, M. & LARS LUND 1999. Simulation of the Peritectic Reactio in 304 Stainless Steel. *Materials Transactions, JIM,* 40**,** 567-570.

JACQUES, P., GIRAULT, E., CATLIN, T., GEERLOFS, N., KOP, T., VAN DER ZWAAG, S. & DELANNAY, F. 1999. Bainite transformation of low carbon Mn–Si TRIP-assisted multiphase steels: influence of silicon content on cementite precipitation and austenite retention. *Materials Science and Engineering: A,* 273-275**,** 475-479.

KERR, W., CISSE, J. & BOLLING, G. F. 1974. On equilibrium and non-equibrium peritectic transformation. *Acta Metallurgica,* 22**,** 677-686.

KIM, H. S., KOBAYASHI, Y. & NAGAI, K. 2006. Simulation of the influence of phosphorus on the prior austenite grain size of high-impurity steels. *Acta Materialia,* 54**,** 2441-2449.

KOZESCHNIK, E. & BHADESHIA, H. K. D. H. 2008. Influence of silicon on cementite precipitation in steels. *Materials Science and Technology,* 24**,** 343-347.

KURZ, W. & FISHER, D. J. 1986. *Fundamentals of Solidification,* Aedermannsdorf, Trans Tech Pub.

LEE, B. J. 1998. Computer Simulation of Diffusional Transformation in Alloy Systems. 한국표준과학연구원(KRISS).

LEE, H. M., BAE, J. S., SOH, J. R., KIM, S. K. & LEE, Y. D. 1998. Diffusional Solidification Behavior in 304 Stainless Steel. *Materials Transactions, JIM,* 39**,** 633-639.

LEE, S. M. 2008. *The change of the morphology of MnS inclusions in steel during unidirectional solidification.* PhD, POSTECH.

LESLIE, W. & RAUCH, G. 1978. Precipitation of carbides in low-carbon Fe-AI-C alloys. *Metallurgical and Materials Transactions A,* 9**,** 343-349.

MAHIEU, J., DE COOMAN, B. & CLAESSENS, S. 2001. Galvanizability of high-strength steels for automotive applications. *Metallurgical and Materials Transactions A,* 32**,** 2905-2908.

MAHIEU, J., MAKI, J., COOMAN, B. C. D. & CLAESSENS, S. 2002. Phase Transformation and Mechanical Properties of Si-Free CMnAl Transformation-Induced Plasticity-Aided Steel. *Metallurgical and Materials Transactions A,* 33A**,** 2573-2580.

MCDONALD, N. & SRIDHAR, S. 2003. Peritectic reaction and solidification in iron-nickel alloys. *Metallurgical and Materials Transactions A,* 34**,** 1931-1940.

MCDONALD, N. & SRIDHAR, S. 2005. Observations of the advancing δ-ferrite/γ-austenite/liquid interface during the peritectic reaction. *Journal of Materials Science,* 40**,** 2411-2416.

MEYER, M. D., VANDERSCHUEREN, D. & COOMAN, B. C. D. 1999. The Influence of the Substitution of Si by Al on the Properties of Cold Rolled C-Mn-Si TRIP Steels. *ISIJ International,* 39**,** 813-822.

MONDRAG N, J. J. R., TREJO, M. H., ROM N, M. D. J. C. & T., H. S. 2008. Description of the Hypo-peritectic Steel Solidification under Continuous Cooling and Crack Susceptibility. 48**,** 454-460.

NATSUME, Y., SHIMAMOTO, M. & ISHIDA, H. 2010. Numerical Modeling of Microsegregation for Fe-base Multicomponent Alloys with Peritectic Transformation Coupled with Thermodynamic Calculations. *ISIJ International,* 50**,** 1867-1874.

PHELAN, D., REID, M. & DIPPENAAR, R. 2006. Kinetics of the Peritectic Phase Transformation: *In-Situ* Measurements and Phase Field Modeling. *Metallurgical and Materials Transactions A,* 37**,** 985-994.

SAMEK, L., DE MOOR, E., PENNING, J. & DE COOMAN, B. 2006. Influence of alloying elements on the kinetics of strain-induced martensitic nucleation in low-alloy, multiphase high-strength steels. *Metallurgical and Materials Transactions A,* 37**,** 109-124.

SHIBATA, H., ARAI, Y., SUZUKI, M. & EMI, T. 2000. Kinetics of peritectic reaction and transformation in Fe-C alloys. *Metallurgical and Materials Transactions B,* 31**,** 981-991.

STEFANESCU, D. M. 2002. *Science and Engineering of Casting Solidification,* New York, Kluwer Academic / Plenum Publishers.

UESHIMA, Y., MIZOGUCHI, S., MATSUMIYA, T. & KAJIOKA, H. 1986. Analysis of solute distribution in dendrites of carbon steel with δ/γ transformation during solidification. *Metallurgical and Materials Transactions B,* 17**,** 845-859.

WON, Y.-M. & THOMAS, B. 2001. Simple model of microsegregation during solidification of steels. *Metallurgical and Materials Transactions A,* 32**,** 1755-1767.

YI, H. L. 2010. *δ-TRIP Steel.* PhD Thesis, POSTECH, Korea.

YI, H. L., GHOSH, S. K., LIU, W. J., LEE, K. Y. & BHADESHIA, H. K. D. H. 2010. Non-equilibrium solidification and ferrite in δ-TRIP steel. *Materials Science and Technology,* 26**,** 817-823.

Acknowledgement

I would like to express my gratitude to Professor Dong-Woo Suh and Bhadeshia, H.K.D.H. for supervision, guidance and enthusiasm. I wish to thank CML members as well as PT group members for their help and friendship. Also, I would like to thank to all of my friends for making my stay at school enjoyable and comfortable.

Lovely thanks to Ki-hyon for his love, care and support.

Finally, I would like to take this opportunity to express my thanks to my family for their love, understanding and support.

Curriculum Vitae

Name: Choi Young-Joo

E-mail: dudwn474@postech.ac.kr

Data of birth: 9th August, 1985

Place of birth: Seoul, South Korea

Education

M. S. 2012, POSTECH (Pohang, Korea), Graduate Institute of Ferrous Technology, Computational Metallurgy Group

B. S. 2009, POSTECH (Pohang, Korea), Department of Materials Science and Engineering